Impacts of M9 Cascadia Subduction Zone Earthquake and Seattle Basin on Performance of RC Core-Wall Buildings

Nasser A. Marafi[1], Andrew J. Makdisi[2], Marc O. Eberhard[3], and Jeffrey W. Berman[4]

The performance of tall reinforced-concrete core building archetypes in Seattle was evaluated for 30 simulated scenarios of an **M**9 Cascadia Subduction Zone interface earthquake. Compared with typical MCE_R motions, the median spectral accelerations of the simulated motions were higher (15% at 2s), and the spectral shapes were more damaging, because the Seattle basin amplifies ground-motion components in the period range of 1.5 s to 6 s. The National Seismic Hazard Maps do not explicitly take into account this effect. The significant durations were much longer (~115 s) than typical design motions because the earthquake magnitude is large. The performance of 32 building archetypes (ranging from 4 to 40 stories) was evaluated for designs that barely met the minimum ASCE 7-10 and 7-16 code requirements, and for more rigorous designs that were typical of current tall building practice in Seattle. Even though the return period of the **M**9 earthquake is only 500 years, the maximum story drifts for the **M**9 motions were on average 11% larger and more variable than those for the MCE_R design motions that neglect basin effects. Under an **M**9 event, the collapse probability for the code-minimum archetypes averaged 33% and 21% for the ASCE 7-10 and 7-16 minimum-designed archetypes, respectively. In contrast, the collapse probability for the archetypes designed according to current tall building practice in Seattle were lower and averaged 19% and 11% for the ASCE 7-10 and 7-16 archetypes, respectively. These collapse probabilities for an **M**9 earthquake, which has a return period of about 500 years, exceeded the target 10% collapse probability in the MCE_R, which has a longer return period.

Keywords: Cascadia subduction zone, reinforced concrete walls, nonlinear dynamic analysis, basin effects, long duration motions

---

[1]Postdoctoral Research Associate, Department of Civil and Environmental Engineering, University of Washington, Seattle, WA 98195

[2]Graduate Research Assistant, Department of Civil and Environmental Engineering, University of Washington, Seattle, WA 98195

[3]Professor, Department of Civil and Environmental Engineering, University of Washington, Seattle, WA 98195

[4]Professor, Department of Civil and Environmental Engineering, University of Washington, Seattle, WA 98195

Introduction

Geologic evidence indicates that the Cascadia Subduction Zone (CSZ) is capable of producing large-magnitude, megathrust earthquakes at the interface between the Juan de Fuca and North American plates (Atwater et al. 1995, Goldfinger et al. 2012). These events are expected to have an average return period of about 500 years (Petersen et al. 2002), which is considerably less than the 2475-year return period for the Maximum Considered Earthquake (MCE), or the approximately 2000-year return period for risk-adjusted MCE (MCE_R) in Seattle. The most recent large-magnitude, interface earthquake on the CSZ occurred in 1700 (Atwater et al. 1995), and according to Petersen et al. (2002), there is a 10-14% chance that a magnitude-9 (**M**9) earthquake will occur along the Cascadia Subduction Zone within the next 50 years.

There has been much uncertainty about the characteristics of the ground motions that would result from a large-magnitude, interface CSZ earthquake, because no seismic recordings are available from such an event. To compensate for the paucity of recorded interface events, Frankel et al. (2018a) simulated the generation and propagation of **M**9 CSZ earthquakes for thirty rupture scenarios, and Wirth et al. (2018) evaluated the sensitivity of the generated motions to the rupture model parameters. These scenarios represent **M**9 full-length ruptures of the CSZ, with variations in the hypocenter location, inland extent of the rupture plane, and locations of high stress-drop subevents along the fault plane. The extent of the down-dip rupture was varied to be consistent with the logic tree branches for a full-length rupture of the CSZ used in the U.S. National Seismic Hazard Maps (NSHM, Peterson et al. 2014).

For frequencies up to 1 Hz, the motions were generated using a finite-difference code (Liu & Archuleta 2002) and a 3D seismic velocity model (Stephenson et al. 2017) that reflects the geological structure of the CSZ and the Puget Lowland region. This region is founded on glacial deposits that overlay sedimentary rocks, which fill the troughs between the Olympic and the Cascade mountain ranges. The model includes several deep sedimentary basins within the Puget Lowland region, including the Seattle basin, which is the deepest. The current NSHM does not explicitly account for the Seattle basin.

A one-dimensional measure of the basin depth is the depth to very stiff material with a shear-wave velocity (V_S) of 2.5 km/s, denoted as $Z_{2.5}$. Campbell and Bozorgnia (2014) used this measure of basin depth in their ground-motion model (GMM) for crustal earthquakes. Figure 1 shows the variation of $Z_{2.5}$ within the Puget Lowland region, in which $Z_{2.5}$ ranges from 4 to 5 km over a wide area. Seattle and its nearby suburbs are located above the Seattle basin, a region where $Z_{2.5}$ reaches values of up to 7 km. The map also shows that there are shallower basins near Everett (north of Seattle) and Tacoma (south of Seattle). In contrast, $Z_{2.5}$ is approximately 0.5 km for a reference outside-basin location, La Grande, WA.

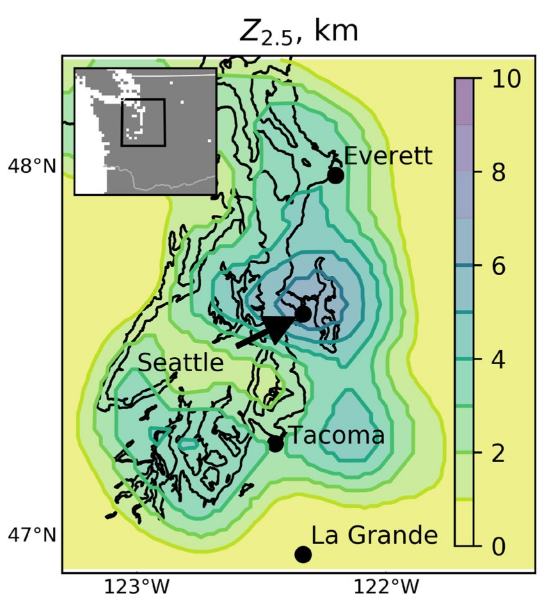

Figure 1. Map of $Z_{2.5}$ for the Puget Lowland Region

For frequencies above 1 Hz, the motions were generated with a stochastic procedure (Frankel, 2009) assuming a generic rock site profile (Boore and Joyner 1997) without considering basin effects. To create a broadband motion, the low-frequency and high-frequency components of the simulated motions were combined using third-order, low-pass and high-pass Butterworth filters, respectively, at 1 Hz.

Figure 2 illustrates the results of one rupture scenario with an epicenter off the coast of Oregon. The figure illustrates the velocity field of the seismic wave propagation across the Pacific Northwest, as well the velocity time history for two locations in Washington State (Seattle and La Grande), at 47 s and 205 s after the initial earthquake rupture. Each scenario generated 500,000 motions on a 1-by-1 km grid spacing for a region ranging from Northern California to Vancouver Island, and from off the West Coast to as far inland as the Cascade mountains. High-resolution (1-by-1 km for the Puget Sound region) and low-resolution (20-by-20 km for the entire model) ground-motion datasets are publicly available (https://doi.org/10.17603/DS2WM3W) from DesignSafe, a data archive supported by the National Science Foundation (Frankel et al. 2018b).

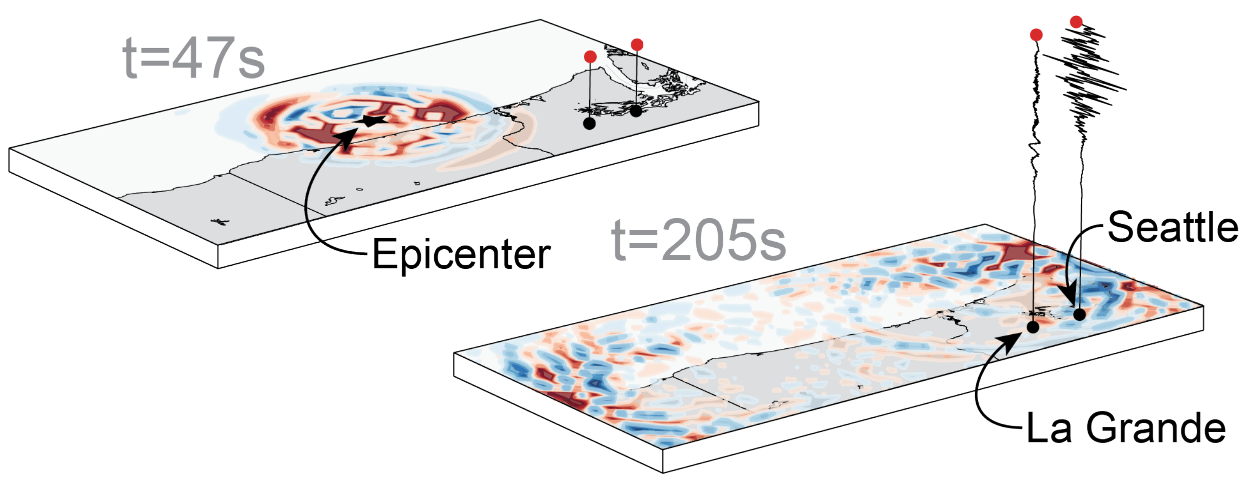

*Figure 2. **M**9 CSZ earthquake scenario showing velocity time history for Seattle and La Grande, Washington at 47s and 205s after the initial earthquake rupture.*

This paper evaluates the impact of the simulated motions on the response of reinforced concrete core wall building archetypes designed for Seattle using ASCE 7-10 (2013) and ASCE 7-16 (2017) provisions with prescriptive and performance-based design approaches. For each code version, one archetype performance group was developed that represents designs that barely meet the minimum code requirements. A second archetype performance group was developed that reflects typical practice for tall buildings in Seattle, i.e., buildings over 73m (240ft), which includes performance-based design considerations. The response of these archetypes to the simulated motions are compared with the response to ground motions selected and scaled to match the risk-adjusted MCE conditional mean spectrum (CMS) for crustal, intraslab, and interface earthquake sources that contribute to the seismic hazard in Seattle. Uncertainty in the drift capacity of the gravity slab-column connections are taken into account in the estimate of the archetype's collapse vulnerability. Finally, collapse probabilities under the **M**9 CSZ scenarios are compared with the motions representing the MCE_R earthquakes, which target a 10% probability of collapse (e.g., FEMA P695, Luco et al., 2007).

Spectral Acceleration of the M9 Ground Motions

In the United States, equivalent-linear seismic design loads (e.g., ASCE 7-10, ASCE 7-16, AASHTO 2017) are derived from the spectral acceleration (for a damping ratio of 5%) at the fundamental period of a structure. Figure 3a shows the spectral acceleration (S_a) in the orientation (direction) corresponding to the maximum spectral response ($S_{a,ROTD100}$) versus period for the 30 scenarios for a site in downtown Seattle. At each period, the geometric mean of $S_{a,ROTD100}$ is denoted with a solid black line, and the dashed black lines denote one lognormal standard deviation above and below the mean. For comparison, the design spectrum corresponding to the ASCE 7-16 risk-adjusted maximum considered earthquake (ASCE MCE_R) (assuming Site Class C) is shown with a solid red line.

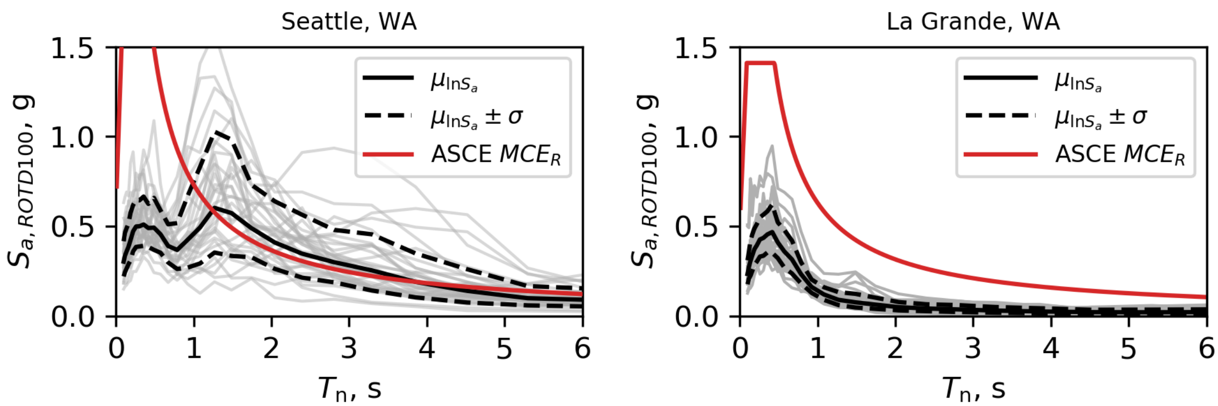

*Figure 3. Maximum direction spectral acceleration for all 30 **M**9 simulations for (a) Seattle and (b) La Grande. Response spectra corresponding to the risk-targeted maximum considered earthquake for Seattle and La Grande (using the 2014 USGS NSHM) are shown in red.*

For Seattle, the spectral accelerations of the **M**9 simulations are smaller than the $\mathrm{MCE_R}$ values for periods below 1 s. However, for periods ranging from 1.5 to 4 s, the geometric mean of the **M**9 spectral accelerations are slightly above the $\mathrm{MCE_R}$ values, and the spectral accelerations for many of the simulated motions greatly exceed the $\mathrm{MCE_R}$ values. For example, 67% (20 of 30) of the motions exceed the $\mathrm{MCE_R}$ values at a period of 2.0 s. This exceedance is important, because the return period for the **M**9 Cascadia event (~500 years) is much shorter than that of the $\mathrm{MCE_R}$ (~2000-year return for Seattle). In addition, **M**9 interface earthquakes represent only part of the seismic hazard in Seattle, which has large contributions from the Seattle Fault and deeper intraslab events. For example, at a period of 2.0 s, the CSZ full-rupture earthquake (**M**8.8 to **M**9.3) contributes only 43% of the total seismic hazard.

Figure 3b shows the same information as Figure 3a but for a reference site 73 km south of Seattle (near La Grande, Washington). This site was selected because La Grande and Seattle have similar values of closest distance to the fault-rupture plane and similar values of the shear-wave velocity in the upper 30 m of the site (V_{S30}). As a result, ground-motion models with no explicit basin terms (e.g., Abrahamson et al. 2016) predict similar spectral accelerations for both locations for an interface earthquake. For periods greater than ~0.7 s, the values of S_a for the simulated motions are much lower for La Grande than for Seattle. The differences between the spectral accelerations of the simulated motions for Seattle and La Grande (Figure 3) can be attributed mainly to the effects of the deep sedimentary basin that underlies Seattle (Marafi et al. 2019b).

Spectral Shape of the M9 Ground Motions

Spectral acceleration does not by itself adequately characterize the effects of ground motions on damage. Numerous researchers have found that the shape of the spectrum at periods near and larger than the fundamental period of the structure affects the response of nonlinear systems, because the fundamental period of a structure elongates as damage progresses. For example, Haselton et al. (2011a), Eads et al. (2015), and Marafi et al. (2016) have shown that spectral shape influences collapse probabilities for structures. Similarly, Deng et al. (2018) developed an intensity measure that accounts for the effects of spectral shape on the ductility demand of bilinear SDOF systems.

Marafi et al. (2016) developed a measure of spectral shape, SS_a, that accounts for the differences in period elongation between brittle and ductile structures, and between low and high deformation demands. This measure correlated well with collapse performance for recorded crustal and subduction earthquake ground motions. SS_a is defined using the integral of the ground-motion response spectrum (damping ratio of 5%) between the fundamental period of the building (T_n) and the nominal elongated period (αT_n). To make SS_a independent of the spectral amplitude at the fundamental period, the integral is normalized by the area of a rectangle with a height of $S_a(T_n)$ and width of $(\alpha-1)T_n$.

$$SS_a(T_n,\alpha) = \frac{\int_{T_n}^{\alpha T_n} S_a(T)dT}{S_a(T_n)(\alpha-1)T_n} \quad (1)$$

where αT_n accounts for the period elongation of the structure. For evaluating the likelihood of exceeding a target displacement ductility, μ_{target}, the upper limit of the period range (αT_n) is taken as equal to the period derived from the secant stiffness; therefore α is taken as $\sqrt{\mu_{target}}$. For evaluating the likelihood of collapse, α is taken as $\sqrt{\mu_{50}}$, where μ_{50} is the displacement ductility at a strength loss of 50% (Marafi et al., 2019a). For two ground motions with similar spectral accelerations that cause yielding, the ground motion with the larger values of SS_a will likely be more damaging than the motion with smaller values of SS_a, because the spectral accelerations are larger at periods above the initial elastic period of the structure.

To compare the spectral shape of the **M**9 motions with those of motions used in current practice for tall buildings (PEER, 2017), conditional mean spectra (Baker 2011) were developed for the MCE_R, denoted as MCE_R CMS. The MCE_R CMS is meant to represent the expected ground motion response spectrum conditioned on the occurrence of a target S_a in the MCE_R at the fundamental period of a structure. To be consistent with current practice in Seattle for tall buildings (Chang et al. 2014), these conditional mean spectra were scaled to include basin amplifications as calculated with the Campbell and Bozorgnia (2014) basin term assuming a value of $Z_{2.5}$ = 7 km for Seattle. The resulting basin amplification factors applied to the CMS ranged from 1.23 at a period of 0.01s to 1.74 at a period of 8 s.

As an example, Figure 4 shows the response spectra for 100 motions selected and scaled to the MCE_R CMS at 2.0 secs, adjusting from geometric mean to maximum direction ground motions (Shahi and Baker 2011) and accounting for basin effects with amplification factors for crustal earthquakes (Campbell and Bozorgnia 2014). Crustal, intraslab and interface motions were included in each ground motion set in proportion to their contribution to the overall seismic hazard at each period. At a period of 2.0 seconds, 47, 6, and 47 motions were used to represent the contribution of the crustal, intraslab and interface events, respectively. Marafi (2018) provides details of the process used to select and scale these motions.

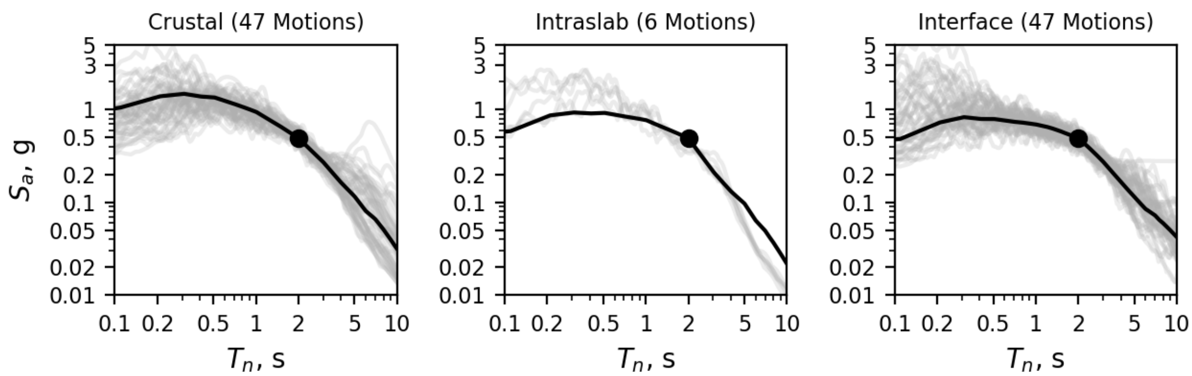

Figure 4. Ground motions selected and scaled to the target 2475-year return conditional mean spectrum at 2.0 s for crustal, intraslab, and interface earthquakes.

For a downtown Seattle site, Figure 5 compares the geometric mean of SS_a of the 30 simulated **M**9 ground motions with that of the 100 MCE_R CMS motions. The spectral shapes for the Seattle **M**9 motions are more damaging (larger SS_a) up to a period of about 4 s. The differences are particularly large in the range of 0.5 s to 3.0 s. These differences are consistent with the response spectra shown in Figure 3. For example, the spectral acceleration in Seattle reaches a maximum at a period of about 1.5 s, so SS_a is above 1.0 near a period of 1.0 s. Periods above 1.5 s have decreasing spectral accelerations, which leads to values of SS_a below 1.0. The **M**9 La Grande motions have even more damaging shapes at long periods, but that difference is unimportant because the spectral accelerations are low for that location.

Duration of M9 Ground Motions

The duration of the ground motion can also affect structural response (e.g., Marsh and Giannotti 1995, Bommer et al. 2004, Raghunandan et al. 2015, Chandramohan et al. 2016). Bommer et al. (2004) found that the effects of duration are pronounced in structures that undergo strength and stiffness degradation with cyclic loading. Hancock and Bommer (2007), and Chandramohan et al. (2016) found that significant duration, D_s, correlated well with structural collapse, and this measure has the advantage of being independent of ground-motion amplitude.

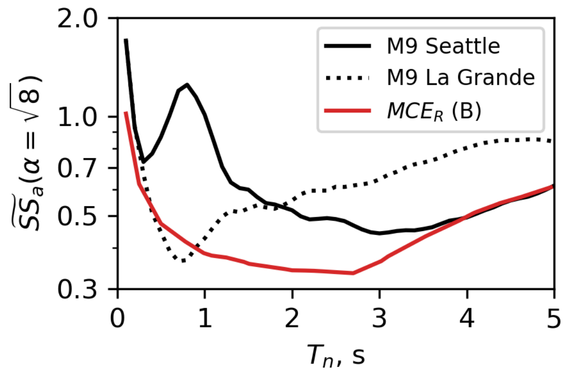

*Figure 5. SS_a ($\alpha = \sqrt{8}$) with respect to period for **M**9 Seattle and motions selected to match the MCE_R CMS considering basins, denoted as MCE_R (B).*

Figure 6 shows the frequency histograms (in log-scale) for D_s computed using the 5-95% Arias intensity time interval ($D_{s,5\text{-}95\%}$) for the 30 simulated **M**9 CSZ motions for Seattle, 66 motions measured during the **M**9 Tohoku earthquake, and 78 motions from FEMA P695 (2008) (typical of design motions for crustal earthquakes). The geometric mean of $D_{s,5\text{-}95\%}$ for the simulated **M**9 CSZ ground motions for Seattle is 115s, which is nearly 30% larger than that of the **M**9 Tohoku earthquake (89 s) motions, considering stations between 100 and 200 km from the earthquake source. Both of these durations are much longer than the FEMA P695 (2008) ground motions, which have a geometric mean of 13s.

The log-normal standard deviation of $D_{s,5\text{-}95\%}$ was 0.21 for the **M**9 Seattle motions, 0.15 for the Tohoku earthquake, and 0.51 for the FEMA motions. These differences are consistent with expectations. The standard deviation is smaller for the Tohoku earthquake than the simulations because the Tohoku motions were recorded for a single event, whereas the simulated motions were derived from 30 scenarios. The standard deviation is largest for the FEMA motions because this set is comprised of motions from distinct events with a wide range of magnitudes and source-to-site distances.

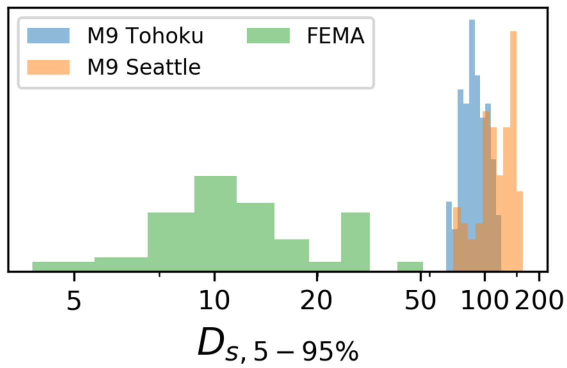

Figure 6. Frequency histograms of $D_{s,5\text{-}95\%}$ for FEMA P695 motions, ***M****9 Tohoku motions recorded at stations with a source-to-site distance between 100 and 200 km, and* ***M****9 CSZ Simulated motions in Seattle.*

Archetype Development

The effects of the **M**9 simulated motions were evaluated for 32 modern, mid- and high-rise reinforced concrete core-wall archetypal residential buildings, ranging from 4 to 40 stories. To reflect current practice in Seattle, all of the archetypes were designed and detailed as special reinforced concrete shear walls (Chapter 18 of ACI 318-14), with a seismic force-reduction factor (R) of 6. The archetypes were developed with the assistance of members of the Earthquake Engineering Committee of the Structural Engineers Association of Washington.

Archetype Layout

Figure 7a shows typical floor plans for the archetypes. The floor plate was 30.5 m (100 ft.) long by 30.5 m (100 ft.) wide with three 9.15 m (30 ft.) bays of slab-column gravity framing in each orthogonal direction. The 4-story archetypes had two planar walls in each orthogonal direction. Archetypes with 8 stories or more used a central core-wall archetype that was symmetrical in both directions, in which one direction used two uncoupled C-shaped walls, whereas the other direction used coupled C-shaped walls. As is typical for residential buildings, the 4- and 8-story archetypes included 2 and 3 basement levels, respectively, and the taller archetypes had 4 basement levels. The basements were assumed to have plan dimensions of 48.8 m x 48.8 m (160 ft x 160 ft) (Figure 7b).

PERFORMANCE GROUPS

Four strategies were implemented (resulting in four performance groups) to design a total of 32 archetypical buildings. Six buildings, ranging from 4 to 24 stories, were designed to barely meet the minimum prescriptive, equivalent lateral-force (ELF) requirements of ASCE 7-10 (2013), following the modal response spectrum analysis (MRSA) procedure. Another six buildings were designed similarly but following the minimum requirements of ASCE 7-16. For both of these performance groups, the maximum allowable drift was 2% for the design earthquake loads, and the flexural demand-to-capacity ratio was near 1.0 at the ground floor. These sets of archetypes are referred to as "code-minimum" performance groups.

The City of Seattle (Director's Rule 5, 2015) requires that buildings with a height above 73 m (240 ft), which corresponds to about 24 stories in a residential building, be evaluated with performance-based design (PBD) procedures. To reflect current practice, 10 buildings, with 4 to 40 stories, were preliminarily designed to satisfy: (a) a stricter drift target of 1.25% under the ASCE 7-10 design loads using MRSA, and (b) a higher flexural demand-to-capacity ratio of 1.25. For buildings 24-stories and taller, nonlinear analysis was performed on the resulting designs to check the strain, force, and drift limits of the Tall Building Initiative (2017) guidelines (TBI). In many cases, the nonlinear checks were satisfied without further modifying the archetypes, but in a few cases, the flexural reinforcement ratio was increased (especially in the upper stories) to satisfy the TBI strain limits. Another 10 buildings were designed similarly, using the ASCE 7-16 provisions. These two sets of archetypes are referred to as "code-enhanced" performance groups.

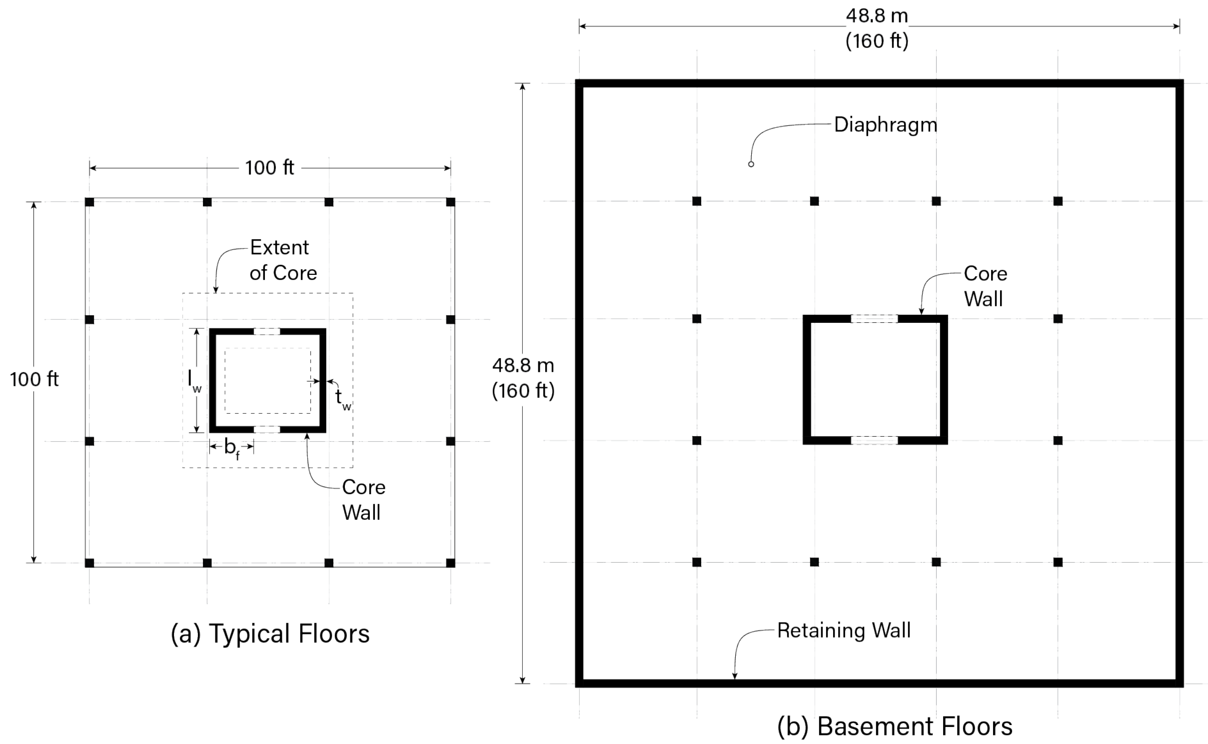

Figure 7. Archetype typical floor plans for the (a) typical floors and (b) basements.

DESIGN LOADS

The seismic weight was assumed to consist of the weight of the core wall, the weight of the gravity system, and the superimposed dead loads (e.g., mechanical equipment, ceilings and partitions). The gravity system and superimposed loads were modeled as a uniform load of 6.2 kPa (130 psf), 11.0 kPa (230 psf), 7.4 kPa (155 psf) for typical, ground, and basements levels, respectively. Uniformly distributed live loads of 2.4 kPa (50 psf), 4.8 kPa (100 psf), 1.9 kPa (40 psf) for typical, ground, and basements levels, respectively, were assumed in the ASCE-7 load combinations.

All of the archetypes were assumed to be founded on glacially-compacted sediments that are common in the Puget Sound region. In Seattle, this material typically has a shear-wave velocity

(V_{S30}) near 500 m/s, which corresponds to NEHRP Site Class C (BSSC 2009). For the ASCE 7-10 archetypes, the design short-period spectral acceleration, S_{DS}, was 0.94g, and the 1-s spectral acceleration, S_{D1}, was 0.42 g. The design accelerations for the ASCE 7-16 archetypes were 19% and 12% higher, respectively (S_{DS} =1.12 g; S_{D1} = 0.49 g). This increase was attributable to changes in seismic hazards maps (NSHM) and site-amplification factors (FEMA 2015). All archetypes were assumed to fall into occupancy Risk Category II, which corresponds to Seismic Design Category D.

ASCE-7 AND ACI 318 DESIGN PROCESS

The design process for all of the archetypes is summarized in Figure 8. The seismic forces induced in the core wall were computed using MRSA, in which the total seismic base shear was determined using ASCE 7 §12.8. Note that the MRSA procedure differed between the two standards; ASCE 7-10 permits a 15% reduction in the lateral-design loads under MRSA, whereas ASCE 7-16 does not.

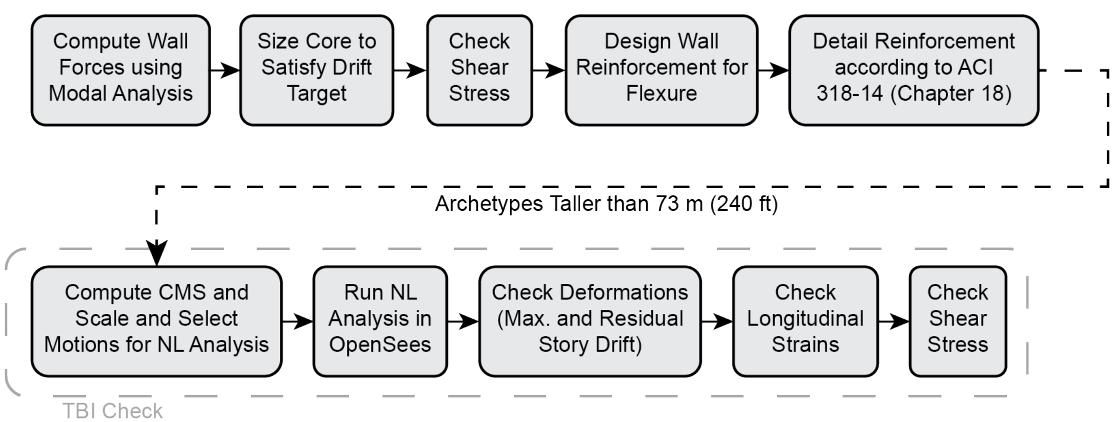

Figure 8. Archetype design flow chart

All core-wall archetypes were designed and detailed according to Chapter 18 in ACI 318-14. The core wall concrete was assumed to have a specified compressive strength (f'_c) of 55.2 MPa (8,000 psi) and reinforced with ASTM A706 steel, which has a nominal yield stress (f_y) of 414

MPa (60 ksi). The sizes and thicknesses of the wall and the reinforcement layout was determined by meeting the following criteria:

(1) Satisfy drift limit (using MRSA, according to ASCE 7-10 §12.12) assuming an effective stiffness of $0.5E_cI_g$, as permitted in ACI 318-14. This drift limit was 2.0% for the code-minimum performance group, whereas it was 1.25% for the code-enhanced performance group, as recommended by the archetype development committee.

(2) Check that the base-shear stress demand resulting from the MRSA demands are less than $0.33\sqrt{f_c'}$ MPa ($4\sqrt{f_c'}$ psi) for the code-minimum design, and are less than $0.17\sqrt{f_c'}$ MPa ($2\sqrt{f_c'}$ psi) in the code-enhanced designs, and

(3) Provide adequate flexural strength, such that $\phi M_n > M_u$ where $\phi = 0.9$; M_n corresponds to the nominal flexural strength (considering interaction between axial load and flexural strength) as per ACI, and M_u is the moment demand as per ASCE 7. The demand-to-capacity ratio ($M_u/\phi M_n$) was approximately 1.0 for the code-minimum performance groups and 0.8 for the code-enhanced groups.

The wall length, measured as the distance between the inner flange faces (l_w - $2t_w$) and flange width (b_f), was kept constant through the height of the archetypes. The wall thickness varied approximately every 12 stories (as recommended by the archetype committee). Consequently, the overall wall length (l_w in Figure 7) also varied slightly along the height.

NONLINEAR PERFORMANCE CHECKS

For archetypes taller than 73.2 m (240 ft), nonlinear time history analyses were performed, and the demands were checked with the limits specified in the 2017 Tall Building Initiative Guidelines (denoted as TBI check in Figure 8). These archetypes were subjected to ground motions selected and scaled to the MCE_R CMS (Marafi et al. 2019a) as per Chapter 16 in ASCE 7-16. To be consistent with current practice for tall buildings in Seattle (Chang et al. 2014), the MCE_R CMS spectra were scaled to include basin amplification as computed with the Campbell and Bozorgnia (2014) basin term for crustal earthquakes. Marafi (2018) summarizes the results of the TBI performance checks (i.e., peak story drifts, residual drifts, wall axial strains, shear forces) for the archetypes with 24 stories or more.

ARCHETYPE PROPERTIES

Table 1 lists the nomenclature and key properties for the archetype buildings. The resulting seismic weights per unit floor area (excluding the basement levels) ranged from 8.16 kPa (171 psf) for the eight-story, ASCE 7-10, code-minimum archetype (S8-10-M) to 9.81 kPa (205 psf) for the forty-story, ASCE 7-16, code-enhanced archetype (S40-16-E). Table 1 also lists the upper-bound limit on design period (C_uT_a) used to compute C_s and the computed elastic period with cracked concrete properties used in the modal analysis. The total base shear, expressed as a percentage of the total building weight (C_s listed in Table 1), ranged from 4% to 18% depending on the code year and archetype height. The minimum base shear requirement in ASCE 7 controlled for buildings with 24 stories and more for the ASCE 7-10 archetypes, and for 20 stories and more for the ASCE 7-16 archetypes.

Table 1. Key archetype properties

Performance Group	Arch. ID	# of Stories (Basements)	C_uT_a (s)	Computed Period[1] (s)	C_s	W[2] (MN)	$\phi M_n/M_u$[3]	V_u/V_c[3]	Drift Ratio (%)	Axial Load Ratio (P_g/f'_cA_g)
Code Minimum (ASCE 7-10)	S4-10-M	4(2)	0.45	1.45	0.152	30.6	1.02	1.7	1.91	0.17
	S8-10-M	8(3)	0.75	2.25	0.102	60.8	1.05	1.53	1.74	0.12
	S12-10-M	12(4)	1.02	3.1	0.075	90.9	1.06	1.33	1.77	0.13
	S16-10-M	16(4)	1.26	4.06	0.061	122.1	1.05	1.11	1.88	0.13
	S20-10-M	20(4)	1.49	4.96	0.051	154.6	1.05	0.95	1.93	0.14
	S24-10-M	24(4)	1.71	5.33	0.045	188.8	1.06	0.73	1.8	0.12
Code Minimum (ASCE 7-16)	S4-16-M	4(2)	0.45	1.08	0.183	30.9	1.05	1.74	1.82	0.11
	S8-16-M	8(3)	0.75	1.93	0.109	61.8	1.06	1.49	1.8	0.1
	S12-16-M	12(4)	1.02	2.7	0.08	92.3	1.01	1.32	1.89	0.11
	S16-16-M	16(4)	1.26	3.53	0.065	125.1	1.03	1.05	1.96	0.11
	S20-16-M	20(4)	1.49	4.36	0.055	158.5	1.05	0.92	2.03	0.11
	S24-16-M	24(4)	1.71	5.11	0.049[4]	195	1.04	0.85	2	0.11
Code Enhanced (ASCE 7-10)	S4-10-E	4(2)	0.45	0.99	0.152	30.8	1.32	1.36	1.35	0.12
	S8-10-E	8(3)	0.75	1.51	0.102	61.2	1.17	1.56	1.16	0.11
	S12-10-E	12(4)	1.02	2.15	0.075	92.1	1.18	1.32	1.09	0.13
	S16-10-E	16(4)	1.26	3.02	0.061	122.9	1.18	1.28	1.22	0.15
	S20-10-E	20(4)	1.49	3.91	0.051	154.3	1.19	1.22	1.32	0.16
	S24-10-E	24(4)	1.71	4.37	0.045	189.4	1.5	0.92	1.29	0.14
	S28-10-E	28(4)	1.92	5.17	0.04[4]	223.4	1.44	0.89	1.34	0.16
	S32-10-E	32(4)	2.12	5.74	0.04[4]	260.9	1.32	0.86	1.33	0.15
	S36-10-E	36(4)	2.31	6.23	0.04[4]	295.2	1.2	0.82	1.3	0.15
	S40-10-E	40(4)	2.5	6.7	0.04[4]	334.6	1.18	0.8	1.17	0.15
Code Enhanced (ASCE 7-16)	S4-16-E	4(2)	0.45	0.78	0.183	31.2	1.18	1.36	1.3	0.08
	S8-16-E	8(3)	0.75	1.25	0.109	62.2	1.19	1.49	1.12	0.09
	S12-16-E	12(4)	1.02	2	0.08	93.9	1.19	1.25	1.19	0.1
	S16-16-E	16(4)	1.26	2.36	0.065	129.9	1.19	0.99	1.15	0.1
	S20-16-E	20(4)	1.49	2.95	0.055	164.8	1.19	0.88	1.19	0.1
	S24-16-E	24(4)	1.71	3.53	0.049[4]	201.6	1.48	0.82	1.24	0.11
	S28-16-E	28(4)	1.92	4.09	0.049[4]	240.3	1.27	0.83	1.27	0.11
	S32-16-E	32(4)	2.12	4.62	0.049[4]	281.3	1.19	0.84	1.28	0.11
	S36-16-E	36(4)	2.31	5.13	0.049[4]	324.8	1.19	0.84	1.27	0.12
	S40-16-E	40(4)	2.5	5.55	0.049[4]	364.9	1.17	0.84	1.3	0.12

Notes: [1]Period computed using cracked concrete properties, [2] Building seismic weight only includes stories above ground floor, [3] computed at ground level, [4]Minimum base shear controls

The resulting ratio of horizontal shear force (due to seismic loads) to the concrete shear capacity, V_u/V_c, ranged from 0.53 to 1.56, which is far below the allowable values (i.e., $V_u/V_c \leq 5$). Table 1 lists the resulting axial load ratios, $P_g/(A_g f'_c)$, where P_g is the axial load computed using the 1.0D + 0.5 L load combination, and A_g is the gross cross-sectional area of the wall. The load

P_g was computed as the sum of the self-weight of the concrete core and the gravity load corresponding to the tributary area resisted by the core that is equal to 50% of the total floor area, equaling 464 m^2 (5000 ft^2). The resulting axial load ratios ranged from 8% to 17%.

Archetype Nonlinear Modelling

For all of the archetypes, the seismic performance was assessed using 2D nonlinear models in OpenSees (McKenna, 2016) with earthquake motions applied only in one direction. Two-dimensional nonlinear models were used in OpenSees because of the availability of test data for validation (as described in Marafi et al. 2019a) and robustness in performance prediction at large deformations. It is acknowledged that a 2D representation of core walls neglects the effects of torsion and bi-directional loading. The nonlinear behavior of the wall was modelled using a methodology, originally developed by Pugh et al. (2015), that was calibrated with approximately 30 experimental tests. Marafi et al. (2019a) extended the methodology to use displacement-based beam-column elements with lumped-plasticity fiber sections to capture the axial and flexural nonlinear responses of the RC walls. The modelling was further improved by modifying the stress-strain behavior of the steel fibers to include the cyclic strength degradation (Kunnath et al. 2009) expected during long-duration shaking. In addition, the pre-peak stress-strain relationship of the concrete material model (*OpenSees* Concrete02) was modified to incorporate the Popovics stress-strain relationship (1973). Appendix B provides details of the modelling methodology.

Maximum Story Drift

The maximum story drifts (MSD) for each of the archetypes were computed for: (1) the simulated **M**9 Motions, for both the Seattle and La Grande sites; (2) motions selected and scaled to match the MCE_R CMS (for Seattle), both with and without considering the basin amplification;

and (3) MCE_R-compatible motions selected and scaled to match the conditional mean and variance spectra (CMS+V, Jayaram et al. 2011).

DRIFTS FOR SIMULATED M9 MOTIONS

The 32 archetypes were subjected to the **M**9 CSZ motions for Seattle and La Grande in the orientation that produced the maximum spectral ordinate ($S_{a,\mathrm{RotD100}}$) at each structure's fundamental period (Table 1), consistent with the nonlinear evaluation provisions of ASCE 7-16 (Chapter 16). The relative rotations and strains were usually the largest at the ground level, so that is where the largest amount of damage to the wall would be expected to occur. However, the performance of the gravity slab-column connections, slab-wall connections, facade system, and other non-structural components depend more on the story drift, which tends to increase along the height of RC-core wall buildings.

Figure 9 shows the calculated maximum story drift envelope for a representative eight-story archetype (S8-10-E) and a 32-story archetype (S32-10-E), subjected to the **M**9 Seattle motions. As expected, the story drifts in the basement are near zero because the basement walls are very stiff. In contrast, the maximum story drifts occur near the top stories, because the cantilever walls accumulate rotations over their height.

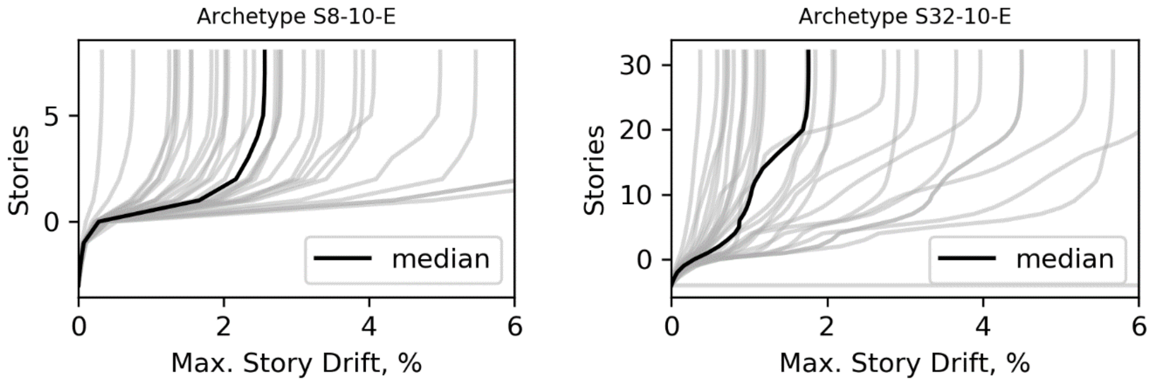

*Figure 9. Distribution of story drift with height for (a) 8-story and (b) 32-story ASCE 7-10 code enhanced archetypes, subjected to Simulated **M**9 Motions in Seattle.*

For all four performance groups, Figure 10 plots the median (computed for each set of 30 motions) of the maximum story drift (computed over the height of each archetype) for the **M**9 CSZ motions in Seattle and La Grande. For Seattle, the maximum drift ratios for the ASCE 7-10 and ASCE 7-16 code-minimum buildings had medians of 3.4% and 2.7%, respectively. In comparison, the TBI guidelines specify a mean maximum story drift limit of 3.0%. The median computed drift ratios exceeded this limit for 5 of the 6 ASCE 7-10 code-minimum archetypes and 2 out of 6 ASCE 7-16 code-minimum archetypes. The drift ratios for the code-enhanced buildings were considerably lower, averaging 1.7% for these two performance groups. None (out of 20) of the code-enhanced designs had median drift ratios that exceeded the TBI limit of 3.0%.

As expected, the story drifts for the **M**9 La Grande motions were much lower. They ranged between 0.2 to 0.5% for all performance groups.

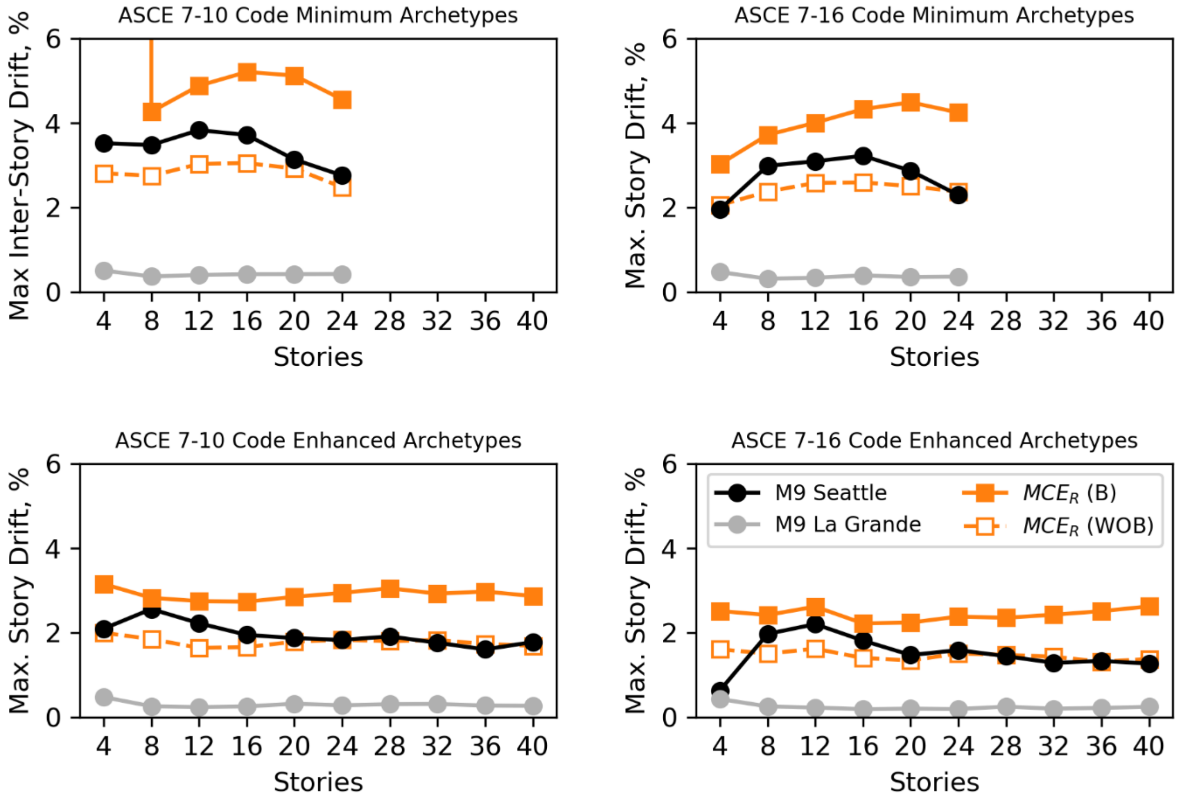

Figure 10. Median of the maximum story drift with respect to archetype story for (a) code-minimum ASCE 7-10 archetypes, (b) code-minimum ASCE 7-16 archetypes, (c) code-enhanced ASCE 7-10 archetypes, and (d) code-enhanced ASCE 7-16 archetypes

COMPARISON WITH DRIFTS FOR MCE$_R$ CMS MOTIONS

The results of the **M**9 simulations can be placed in the context of current design practice by comparing the drift demands with those calculated for earthquake motions matching the MCE$_R$ Conditional Mean Spectra (CMS) (Figure 10). The effects of the basin are neglected by the national seismic hazard maps and in current practice for most buildings shorter than 73.3m (240 ft), so a suite of 100 MCE$_R$ motions were developed without considering the basin (MCE$_R$ WOB). As shown in Figure 10, the TBI drift limit (3%) for the MCE$_R$ motions without considering the basin was satisfied by nearly all the archetypes (only two archetypes exceeded the limit up to 0.5%). On average (over 32 archetypes), the maximum story drifts for the **M**9 motions were on average 1.11 times higher than those for the MCE$_R$ (WOB) motions.

Basins are taken into consideration for the nonlinear evaluation of tall buildings (>240 ft) (Chang et al. 2014), so a second suite of 100 MCE_R motions was developed that accounted for the basin using the Campbell and Bozorgnia (2014) basin amplification term (MCE_R (B)). The computed median of the maximum drift ratios for the **M**9 motions in Seattle were all lower than the drift ratios for the MCE_R (B) "with-basin" motions currently used to evaluate the performance of tall buildings in Seattle. On average (over 32 archetypes), the median of the maximum story drifts for the **M**9 motions were equal to 0.67 times the median of the maximum drifts for the MCE_R (B) motions. For the 4-story ASCE 7-10 Code Minimum archetype, 59% of the MCE_R (B) motions resulted in story drifts that exceeded 10% during the analysis. This is illustrated on Figure 10a as a vertical line (with solid square symbols) prior to the 8-story data point.

COMPARISON WITH Drifts for MCE_R CMS + VARIANCE MOTIONS

The comparisons made in Figure 10 are consistent with the performance-design practice for tall buildings (e.g., TBI 2017), in which the performance of a building is evaluated for its median response for a set of ground motions. However, the variability in the thirty **M**9 simulations is larger than that of the MCE_R CMS motions, because the simulations account for inter-event variability, but the MCE_R CMS motions do not. Unlike the simulations, the CMS process selects and scales motions to fit a target spectrum (Figure 4), representing a "median" event, without considering the variability in the spectra for these motions.

To be consistent with the **M**9 simulations, MCE motions were developed to account for uncertainty of the MCE_R motions. To capture the inter-event uncertainty in the conditional spectra, the MCE_R motions were selected and scaled to match the target mean and variance conditional spectra (CMS+V, Jayaram et al. 2011) in the maximum direction (Shahi and Baker 2011). As an example, Figure 11 shows the response spectra for 100 motions selected to represent the three earthquake source mechanisms for a MCE$_R$ response spectra conditioned at a 2.0 s period. To capture the uncertainty in the response spectra, motions were selected to have spectral ordinates that are within two standard deviations of the target conditional spectra whilst achieving the target mean S_a and target variance at each period. Note that the median values of the motions in Figure 11 are similar to that for Figure 4, but the spectral ordinates (below and above T_n) for the motions vary more. Marafi (2018) provides details of the ground-motion selection and scaling process.

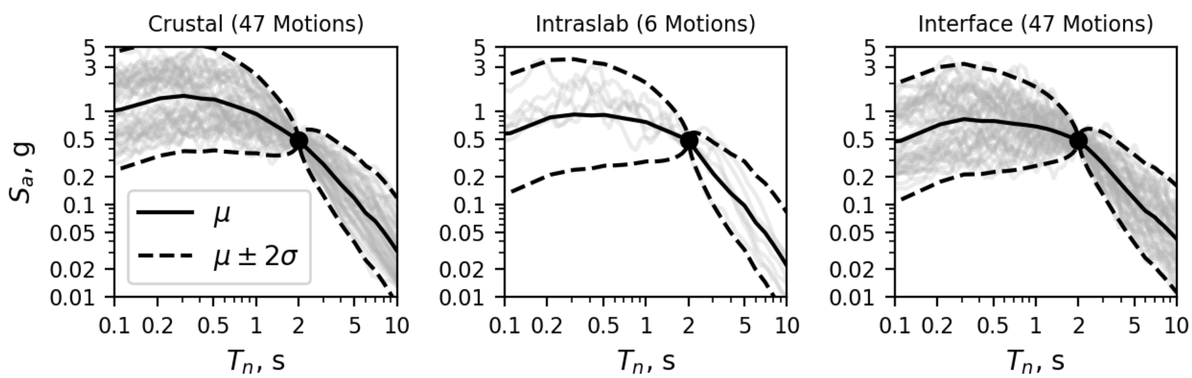

Figure 11. Ground motion targeting mean and variation of the conditional spectrum at 2.0s (corresponding to the period of archetype S12-16-E) for crustal, intraslab, and interface earthquakes.

Figure 12 shows the probability of exceeding a maximum story drift for the 8-story and 32-story ASCE 7-10 code-enhanced archetypes for three ground-motions sets: **M**9 Seattle, MCE$_R$ conditional mean spectra (MCE$_R$ CMS), and MCE$_R$ conditional mean and variance spectra (MCE$_R$ CMS+V), including basin effects. As expected, the maximum story drift corresponding to a 50% probability of exceedance was similar (within ~0.2% drift) between the MCE$_R$ conditional mean spectra (hollow orange dots in Figure 12) and conditional mean and variance spectra (solid orange dots in Figure 12). However, the maximum story drift (MSD) values at the tails of the fragility function (e.g., 16% likelihood of exceedance, one σ below μ) correspond to larger drift levels for the CMS+V motions (4.4% for archetype S32-10-E) than the CMS motions (3.6% for S32-10-E).

The **M**9 simulations have even more variability than the CMS+V motions. For example, consider again archetype S32-10-E. The drift ratio for a probability of exceedance of 16% is 2.57 times the median value for the **M**9 Seattle simulations. The corresponding ratios for the MCE_R CMS+V and CMS motions were 1.43 and 1.24, respectively. These differences are important because they indicate that, even for ground-motion sets with similar median deformation demands, the higher variability in the **M**9 simulated motions would likely translate to a higher risk of severe damage, including collapse.

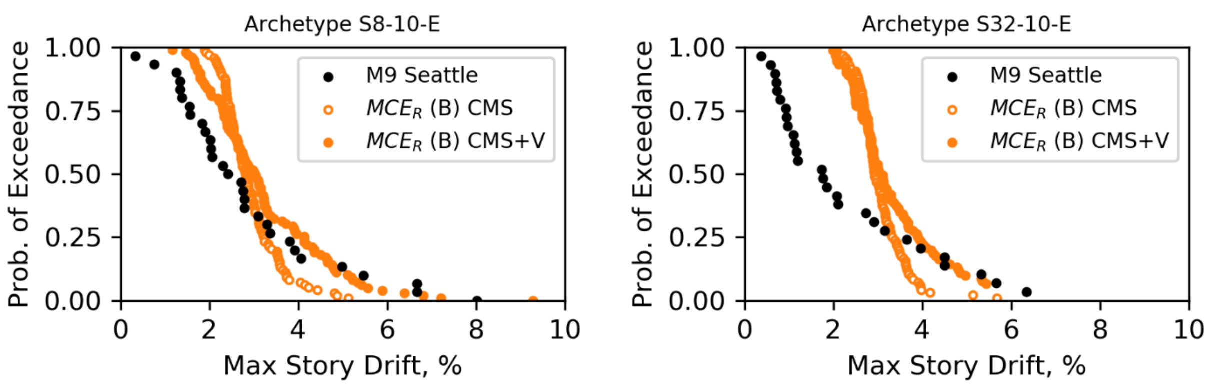

Figure 12. Probability of exceedance with respect to maximum story drift for ASCE 7-10 code-enhanced (a) 8-Story and (b) 32-Story archetypes.

Probability of Collapse

Recent building seismic provisions in the United States have been developed to provide a nominally uniform protection against collapse. The ASCE 7-16 provisions target a 1% likelihood of collapse during a period of 50 years. For an earthquake with a return period of 500 years (neglecting other earthquake sources and assuming a Poisson distribution) the 1% in 50-year target would correspond roughly to a 10% likelihood of collapse during the 500-year event (i.e. $1\text{-}e^{-(0.10/500*50)}) \simeq 0.01$). Coincidentally, the FEMA P695 (2009) guidelines use the same 10% target limit for a population of archetypes subjected to the MCE ground motions.

Building collapse may occur due to a sway mechanism that results in dynamic instability, in which the lateral drift of the building increases essentially without bound (Haselton et al., 2011b) under earthquake shaking. A building may also collapse (or partially collapse) due to the failure of components of the gravity system. Here, both mechanisms are considered in evaluating collapse.

DRIFT CAPACITY OF GRAVITY SYSTEM

The flat plate and flat slab are the most common gravity systems in modern RC core-wall structures. In this paper, the failure of the gravity system was assumed to be triggered by the failure of the slab-column or slab-wall connection. For these systems, integrity slab reinforcement might delay collapse after punching shear failure, but it was not possible to model this phenomena, so these failures were treated as "collapses". Experimental data were used to evaluate the likelihood of collapse of the gravity system for a particular drift demand. Recall that the response of the gravity system was not modeled explicitly, as the stiffness and strength contributions of the gravity system were assumed to be lower compared to that of the lateral system. However, if considered the gravity system can contribute ~10% of the total lateral resistance of the building in some circumstances (SEAW Earthquake Engineering Committee meeting, personal communication, 2018, January 9th).

Hueste et al. (2007 and 2009) found that the drift capacity of slab-column connections depended on: (a) the ratio of shear stress due to gravity loads to the nominal shear-stress capacity provided by the concrete slab (gravity-shear ratio), and (b) the presence of shear reinforcement. To be consistent with design practice, this paper assumes that the archetype's slab-column connections are reinforced with shear studs and have a gravity shear ratio between 0.4 to 0.6. Figure 13 summarizes the data collected by Hueste et al. (2009) on the connection rotations at the failure of slab-column connections (experiments by Dilger and Cao, 1991, Dilger and Brown, 1995, Megally and Ghali, 2000) for all tests that satisfied these two criteria. The data shown in the figure do not include more recent test results reported by Matzke et al. (2015), who considered a bidirectional loading protocol and reported lower drift capacities than those determined from previous tests which considered a unidirectional loading protocol. Figure 13 shows the cumulative distribution (black dots) of the slab-column drift capacity, as well as the corresponding fitted lognormal cumulative distribution (black line). The geometric mean of the drift capacity is 5.9%, and the lognormal standard deviation (σ_{ln}) is 0.12.

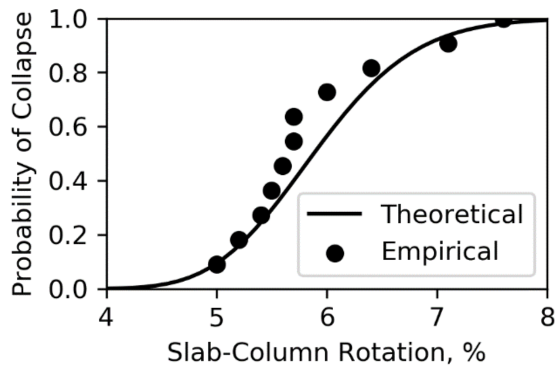

Figure 13. Probability of collapse due to slab-column connection failure with respect to the maximum story drift (for experiments with shear-reinforcements and a gravity shear ratio between 0.4 to 0.6).

Because of limited experimental data, other failure modes in the gravity system are not considered here. Klemencic et al. (2006) showed that the drift capacity of two slab-wall connections exceeded 5% story drift, but the connections were not tested to failure. This paper assumes that the failure would initiate in the slab-column connections.

RACKING DEFORMATIONS

The drift demands on the slab-column connections result from the in-plane rotational deformations of the gravity system bays. These rotations are affected by: (1) the rigid-body rotation of the core wall at the elevation of the floor slab, and (2) the added deformations due to racking effects that result from the difference in vertical deformations between the edge of the core wall and the adjacent gravity-system column, usually located on the perimeter of the building (see Figure 7).

The total relative rotation between the slab-column and edge of wall (due to both of these effects) can be computed as the maximum story drift ratio, MSD, amplified by a racking factor, γ_{rack}. Assuming rigid-body rotation of the wall, and assuming no axial shortening in the gravity system columns, the slab-column rotation, SCR, can be approximated as (Charney 1990):

$$SCR = \gamma_{rack} \cdot MSD = (1 + \frac{l_w}{2l_{bay}}) \cdot MSD \quad (2)$$

where l_w is length of the central core, and l_{bay} is the distance between the face of the core wall and the gravity columns. The length of the core relative to the length of the gravity system bay (for a constant 30.5 m, 100 ft, floor width) varied among the archetypes. Consequently, γ_{rack} varied among the archetypes from 1.11 (Archetype S4-10-M) to 1.56 (Archetype S40-16-E).

COLLAPSE PROBABILITY

For each archetype and ground motion set, the conditional collapse probabilities for a given earthquake event were computed considering the variability in the column-slab rotations (Eq. 3) calculated from the maximum story drift demands (Figure 12), as well as the variation in drift capacity among the scenarios (Figure 13):

$$P[collapse|event] = \sum_{i=1}^{N} P[collapse \mid SCR_i] \; P[SCR_i|event] \quad (3)$$

where N corresponds to the number of scenarios in a set (e.g., **M**9 Seattle, MCE_R with and without basin effects using CMS+V). P[collapse|SCR_i] is the probability of collapse for a given a value of slab rotation for a particular scenario (Figure 13). Assuming that all ground-motion scenarios are equally likely, $P[SCR_i|event]$ = 1/N.

Figure 14 shows the probability of collapse for each archetype, performance group, and ground-motion set. For comparison, the figure also shows the FEMA P695 target value of 10% for the conditional probability of collapse in the MCE_R for an archetype group. Table 2 summarizes the mean and range of the collapse probabilities for all ground-motion sets and archetype performance groups.

For the ASCE 7-16 MCE_R motions developed without considering the effects of the basin (MCE_R WOB) the average collapse probability was near or below the 10% target value. For example, the average collapse probability for ASCE 7-10 and ASCE 7-16 code-minimum archetypes were 13% and 5%, respectively. The average collapse probabilities were even lower for the code-enhanced archetypes (7% and ~0% for the ASCE 7-10 and ASCE 7-16, respectively). These statistics show that the simulated collapse performance of the archetypes is consistent with that expected by the code; the ASCE 7-10 and 7-16 design spectra were developed without considering the effects of basins.

The collapse probabilities were much larger for the basin-modified MCE_R motions, denoted as MCE_R (B). For the ASCE 7-16 code-enhanced archetypes, the collapse probabilities for MCE_R (B) motions were near the target values, with an average value of 12% (Table 2). This result is expected, because the lower target drift ratio (1.25% vs 2.0%) and lower demand-to-capacity ratio are usually used by engineers to satisfy the nonlinear performance evaluation with motions that include a basin factor. The ASCE 7-10 code-enhanced archetypes had higher collapse probabilities, as expected, because the design forces were lower, with collapse probabilities ranging from 11% to 32% (Table 2). In contrast, the collapse probabilities for the code-minimum designs far exceeded the 10% limit, reaching values of 66% and 53% for the ASCE 7-10 and

ASCE 7-16 code-minimum designs. This comparison shows that the basin effect dramatically increases the likelihood of collapse.

The total collapse probability shown in Figure 14 includes scenarios in which story drifts increased without bounds (global instability), as well as the probability of slab-column punching shear failure (Figure 13). The likelihood of global instability (as opposed to punching shear failure) increased as the total likelihood of collapse increased. For example, the global instability mechanism (story drifts >8%) contributed on average 13% of the total collapse probability for all the archetypes with total collapse probability less than 10% (MCE_R (B) ground-motion set). In contrast, the global instability contributed on average 51% of the total collapse probability for all the archetypes with total collapse probability greater than 50%.

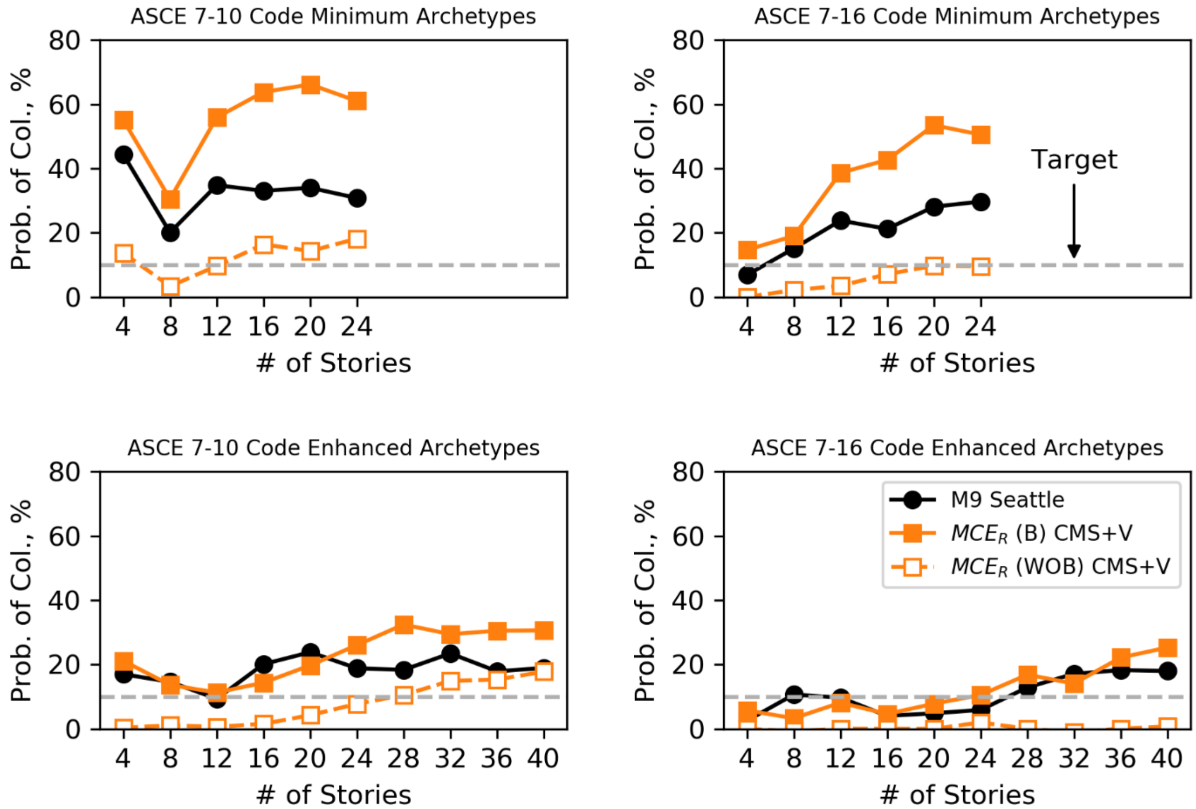

Figure 14. Probability of Collapse with respect to archetype story for (a) code-minimum ASCE 7-10 (10-E) archetypes, (b) code-minimum ASCE 7-16 (16-M) archetypes, (c) code-enhanced ASCE 7-10 (10-E) archetypes, and (d) code-enhanced ASCE 7-16 (16-E) archetypes

Table 2. Summary of Mean and Range of Collapse Probabilities for simulated **M**9 motions in Seattle.

Ground Motion Set	Model Assumption	Code Minimum Archetypes ASCE 7-10		Code Minimum Archetypes ASCE 7-16		Code Enhanced Archetypes ASCE 7-10		Code Enhanced Archetypes ASCE 7-16	
		Mean	Range	Mean	Range	Mean	Range	Mean	Range
M9 Seattle	Racking	33	20-44	21	7-30	18	9-24	10	3-18
	No Racking	27	14-44	16	7-26	11	4-17	3	0-6
MCE$_R$ (B) CMS+V	Racking	55	30-66	37	15-53	23	11-32	12	3-25
	No Racking	40	18-53	23	11-35	13	4-20	6	0-14
MCE$_R$ (WOB) CMS+V	Racking	13	3-18	5	0-10	7	0-18	0	0-2
	No Racking	9	2-13	3	0-7	6	0-14	0	0-2

The collapse probabilities for the **M**9 simulations are not directly comparable to those targeted for the MCE$_R$ earthquake. The return period for the **M**9 motions is much shorter than for the MCE$_R$, and the MCE$_R$ also considers other earthquake sources. Nonetheless, it is instructive to compare the two, because a value of 10% for an **M**9 event represents an upper bound on the acceptable collapse probability. The collapse probabilities for the **M**9 Seattle motions differed greatly, depending on whether the archetypes were designed to code-minimum levels or code-enhanced levels. For the code-enhanced performance groups, the collapse probabilities for the **M**9 Seattle motions were similar to those of the MCE_R (B) motions, with a mean of 11% for the ASCE 7-16 buildings. For the code-minimum groups, the collapse probabilities for the **M**9 motions fell between the values for the MCE_R (WOB) and MCE_R (B) motions. The average collapse probabilities for the ASCE 7-10 and ASCE 7-16 code-minimum buildings were 33% and 21%, which greatly exceed the upper-bound value of 10%.

The average and range of collapse probabilities for each group are summarized in Table 2 for the conditions in which racking is considered or neglected. The trends in collapse probability with number of stories are affected by differences in the racking factors. The racking factors tend to increase with structure height, as the wall size increases whereas the location of the gravity columns remain the same. For example, the S4-16-E four-story archetype had γ_{rack} equal to 1.19, which increased the calculated collapse probability from 2% (no racking) to 6% (with racking). In comparison, the S40-16-E forty-story archetype had γ_{rack} equal to 1.56, which increased the calculated collapse probability from 14% (no racking) to 25% (with racking).

Relating Collapse Probabilities to Ground-Motion Characteristics

The large story drifts (Figure 12) and collapse probabilities (Figure 14) estimated for an **M**9 earthquake in Seattle are attributable to the combined effects of spectral acceleration, spectral shape, and ground-motion duration. A scalar intensity measure, developed by Marafi et al. (2019b), makes it possible to identify and account for the impact of each of these ground-motion characteristics on structural performance. This intensity measure, referred to as the effective spectral acceleration, $S_{a,eff}$, can be computed as:

$$S_{a,eff}\,(T_n) = S_a(T_n) \cdot \gamma_{shape} \cdot \gamma_{dur} \tag{4}$$

where $\gamma_{shape} = \frac{SS_a(T_n,\alpha)}{SS_{a,0}}$ accounts the effects of spectral shape, where $SS_{a,0}$ is taken as ln α / (α - 1), and $\gamma_{dur} = \left(\frac{D_{s,5-95}}{12\,T_n}\right)^{.1}$ accounts for the effects of duration (Marafi 2018).

Collapse fragility functions were derived for all 12 code-minimum archetypes for the M9 Seattle set (30 motions), as well as the MCE_R motions with basin effects and without basin effects (200 motions for each archetype). To be able to compare the effective spectral accelerations among the archetypes, the fragility curves were defined using the normalized intensity measures S_a/η and $S_{a,eff}/\eta$, where η is the base-shear strength (from pushover analysis) normalized by the seismic weight of the structure. Figure 15 shows the average collapse probability for 11 bins (spaced lognormally) and fitted collapse fragilities for the **M**9 Seattle and MCE_R motions.

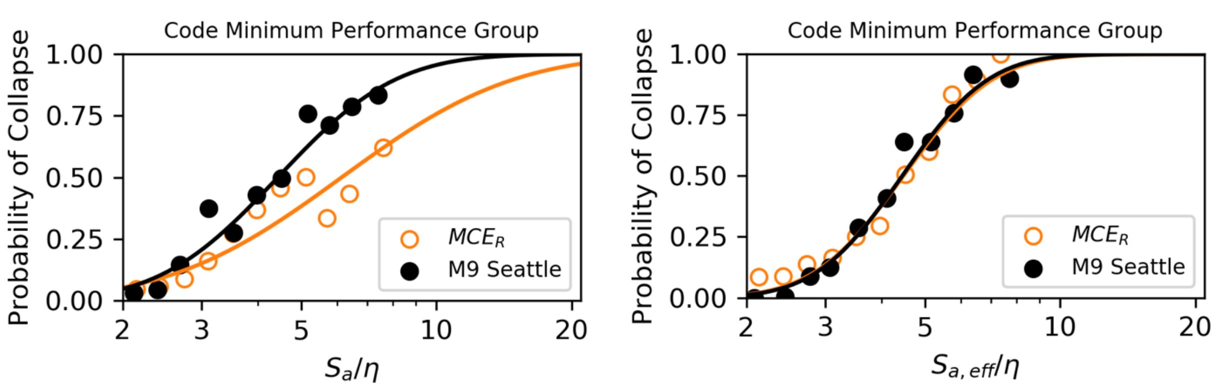

*Figure 15. Collapse fragility for all code-minimum archetypes subjected to **M**9 Seattle motions and MCE_R (with and without basins) with respect to (a) normalized spectral acceleration and (b) normalized effective spectral acceleration.*

The use of $S_{a,eff}$ (as opposed to S_a) as a ground-motion intensity factor improved the estimates of collapse in two ways. As shown in Figure 15a, the likelihood of collapse estimated from S_a differed greatly between the two sets of motions. For example, the value of S_a/η at a collapse probability of 50% (collapse capacity) was 6.15 for the MCE_R motions and 4.43 for the **M**9 Seattle motions, a difference of 29%. By accounting for the effects of spectral shape (Figure 5) and duration (Figure 6) with $S_{a,eff}/\eta$, this difference between collapse capacities reduced to 1% (4.48 for MCE_R and 4.45 for **M**9).

The intensity measure $S_{a,eff}/\eta$ also reduces the uncertainties in collapse prediction within each motion set. This uncertainty is typically quantified using the standard deviation of a log-normal distribution (σ_{ln}). For the **M**9 motions, σ_{ln} was reduced from 0.48 for S_a/η to 0.35 for $S_{a,eff}/\eta$ (a 27% reduction). Similarly, the standard deviation of the fragility curves derived for the MCE_R motions decreased from 0.70 to 0.36, corresponding to a 49% reduction.

The form of $S_{a,eff}$ made it possible to identify the contributions of amplification of spectral acceleration, spectral shape, and duration to ground-motion intensity. Figure 16 shows ratio of the value of each component of $S_{a,eff}$ (S_a, γ_{shape}, γ_{dur}) for the **M**9 motions, divided by the corresponding value for the MCE_R (WOB) CMS+V motions. The contribution of duration was approximately equal to 1.1 for all archetypes. For the shortest (4 stories) and tallest (24 stories), the difference in $S_{a,eff}$ was mainly due to the effects of spectral shape (~1.3). In contrast, the increase in $S_{a,eff}$ was mainly attributable to the effects of spectral acceleration for archetypes with 8 to 16 stories (~1.3). Figure 16 shows (solid grey line) that the combined effects of these three factors led to a nearly constant ratio of $S_{a,eff}$ (1.4 ± 0.18), which in turn explains the nearly constant ratio in collapse probabilities (Figure 14 a and b).

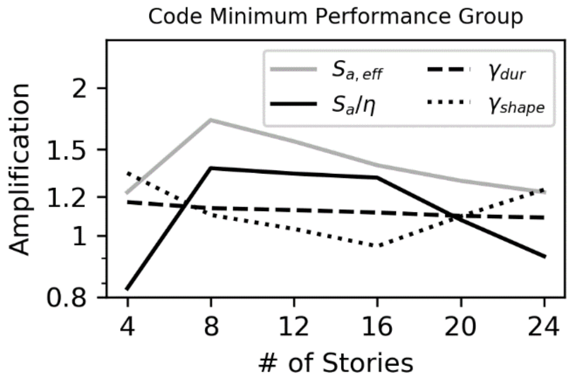

*Figure 16. Ratio of the components of $S_{a,eff}$ (**M**9 to MCE_R (WOB) CMS+V) with respect to number of stories for code-minimum archetypes.*

Other Source of Uncertainty

The previous collapse probability calculations accounted for record-to-record uncertainty among the simulations, and some uncertainty in drift capacity of the gravity system (Figure 13, $\sigma_{\ln}$ = 0.12), but they did not account for other sources of uncertainties. In ASCE 7-16's risk calculations, a total uncertainty (lognormal standard deviation of a collapse fragility) of 0.6 is assumed, which includes a contribution from the record-to-record uncertainty taken as 0.40. The remainder of the included uncertainty (material, design, and modelling uncertainties, FEMA P695) can be approximated as 0.45. To be consistent with the ASCE 7-16 assumptions, the value of the uncertainty in capacity was increased from 0.12 to 0.45.

As expected, increasing the uncertainty (from 0.12 to 0.45 in the collapse fragility in Figure 13) increased the collapse probability for all archetypes. The average collapse probability under an **M**9 increase by 3.5% (33.5% to 37.0%) and 4.7% (21.3% to 26.0%) for the ASCE 7-10 and ASCE 7-16 code-minimum archetypes, respectively. The collapse probability also increased for the ASCE 7-10 and ASCE 7-16 code-enhanced archetypes by 2.3% (18.7% to 21.0%) and 1.6% (10.8% to 12.4%), respectively.

Summary and Conclusions

Thirty physics-based ground-motion simulations (Frankel et al. 2018a) provided the opportunity to evaluate the impacts of an **M**9 CSZ earthquake and the Seattle basin on the performance of reinforced concrete core wall buildings in Seattle. The motions were particularly damaging because: (i) the median spectral accelerations exceeded the MCE_R spectra for periods between 1.5 to 4.0 s (Figure 3), (ii) the median spectral shapes were more damaging (up to a period of 4.0 s) than those typically considered in design (MCE_R CMS, Figure 5), and (iii) the motions were much longer than crustal motions typically considered to evaluate structural systems (FEMA P695, Figure 6). These damaging characteristics were attributed to the effects of the Seattle Basin and the large magnitude of the earthquake.

The impacts of these motions were evaluated for thirty-two archetypes, ranging from 4 to 40 stories, representing modern residential concrete wall buildings in Seattle. Archetypes were developed to reflect the ASCE 7-10 and ASCE 7-16 code provisions, for code-minimum and code-enhanced practice. For all the archetypes, the median (for 30 **M**9 scenarios) of the maximum story drift ratio (for each archetype) exceeded the drift ratio for motions that are consistent with the ASCE 7-16 MCE_R spectra, which do not account for the effects of basins (Figure 10). In addition, the calculated drift ratios for the **M**9 motions varied more than those for the MCE_R motions, even accounting for variance in the conditional spectrum (MCE_R (B) CMS+V, Figure 12).

The average collapse probability for all four performance groups met the 10% collapse probability target for motions that are consistent with the current National Seismic Hazard Maps (MCE_R (WOB) CMS +V, Figure 14), which do not explicitly account for the effects of basin. This result suggests that the archetype design and modeling approaches were consistent with code expectations. In contrast, the collapse probabilities were much larger for motions that considered the effects of the basin (**M**9 and MCE_R (B) CMS +V, Figure 14). For example, the code-minimum, ASCE 7-10 buildings had an average conditional collapse probability of 34% for an **M**9 event. For the code-enhanced, ASCE 7-16 archetypes, the average collapse probability was 11%. The difference in collapse probabilities (Figure 14) were shown to be attributable (using $S_{a,eff}$) to the combined effects of spectral acceleration, spectral shape and duration (Figure 16).

The results presented in this paper are limited to the seismic performance in the uncoupled direction (shown in Figure 7) for ground-shaking in the direction corresponding to the maximum spectral acceleration at the building period. It should be noted that components of RC core wall systems are often coupled and therefore resist induced seismic forces in both orthogonal directions, simultaneously.

In interpreting these results, it is important to consider that the 10% collapse probability target corresponds to an MCE_R event with a return period that is much longer than the 500-year return period for the **M**9 event. In addition, other sources of earthquakes contribute to the hazard in Seattle. Both considerations will further increase the collapse risk. To reduce collapse risk, the seismic design forces could be increased, engineers could modify the allowable drift levels (similar to the code-enhanced designs), or other solutions could be employed to reduce engineering demand and improve system performance. Alternatively, communities could accept higher collapse risks, as has been done in some regions of the U.S. Any of these approaches would have large implications for structural design in the Pacific Northwest.

Acknowledgments

This research was funded by the National Science Foundation under Grant No. EAR-1331412. The computations were facilitated through the use of advanced computational, storage, and networking infrastructure provided by Texas Advanced Computing Center at the University of Texas at Austin and NSF Grant No. 1520817 (NHERI Cyberinfrastructure). The authors would like to thank (a) Steve Kramer for his help using ProShake for site-response analysis, (b) Silvia Mazzoni for sending a large subset of intraslab motions from the PEER NGA-Subduction project, (c) Doug Lindquist from Hart Crowser for providing access to the EZ-Frisk software to run the CMS calculations, and to (d) David Fields and John Hooper from MKA, Andrew Taylor, Brian Pavlovec, and Scott Neuman from KPFF, and Terry Lundeen, Bryan Zagers, and Zach Whitman from CPL, Tom Xia from DCI-Engineers, Clayton Binkley from ARUP, Kai Ki Mow from City of Bellevue, Cheryl Burwell and Susan Chang from City of Seattle for being part of the SEAW Archetype Development Committee. Any opinion, findings, and conclusions or recommendations expressed in this material are those of the authors and do not necessarily reflect the views of the collaborators or sponsoring agencies.

References

Abrahamson, Norman, Nicholas Gregor, and Kofi Addo. 2016. "BC Hydro Ground Motion Prediction Equations for Subduction Earthquakes." *Earthquake Spectra* 32(1): 23–44. http://earthquakespectra.org/doi/10.1193/051712EQS188MR (April 21, 2016).

American Concrete Institute (ACI). 2014. "318-14: Building Code Requirements for Structural Concrete and Commentary."

ATC (Applied Technology Council). 2018. *Improving Seismic Design of Buildings with Configuration Irregularities (ATC-123)*.

ASCE. 2013. *Minimum Design Loads for Buildings and Other Structures*. ed. American Society of Civil Engineers. Reston, Virginia: Published by American Society of Civil Engineers.

ASCE. 2014. *Seismic Evaluation and Retrofit of Existing Buildings (ASCE/SEI Standard 41-13).* Structural Engineering Institute, American Society of Civil Engineers, Reston, VA.

ASCE. 2017. *Minimum Design Loads and Associated Criteria for Buildings and Other Structures, ASCE/SEI 7-16.* Reston, VA: American Society of Civil Engineers.

AASHTO. 2017. *LRFD Bridge Design Specifications*. American Association of State Highway and Transportation Officials.

Atwater, B. F., Nelson, A. R., Clague, J. J., Carver, G. A., Yamaguchi, D. K., Bobrowsky, P. T., Bourgeois, J., Darienzo, M. E., Grant, W. C., Hemphill-Haley, E., Kelsey, H. M., Jacoby, G. C., Nishenko, S. P., Palmer, S. P., Peterson, C. D., and Reinhart, M. A. 1995. "Summary of Coastal Geologic Evidence for Past Great Earthquakes at the Cascadia Subduction Zone." *Earthquake Spectra*, 11(1), 1–18.

Baker, Jack W. 2011. "Conditional Mean Spectrum: Tool for Ground-Motion Selection." *Journal of Structural Engineering* 137(3): 322–31. http://ascelibrary.org/doi/10.1061/%28ASCE%29ST.1943-541X.0000215.

Birely, Anna C. 2012. "Seismic Performance of Slender Reinforced Concrete Structural Walls." University of Washington.

Bommer, Julian J, Guido Magenes, Jonathan Hancock, and Paola Penazzo. 2004. "The Influence of Strong-Motion Duration on the Seismic Response of Masonry Structures." *Bulletin of Earthquake Engineering* 2(1): 1–26. http://link.springer.com/10.1023/B:BEEE.0000038948.95616.bf (August 17, 2015).

Boore, D M, and W b. Joyner. 1997. "Site Amplifications for Generic Rock Sites." *Bulletin of the Seismological Society of America* 87(2): 327–41.

Building Seismic Safety Council (BSSC). 2009. *NEHRP Recommended Seismic Provisions for New Buildings and Other Structures (FEMA P-750)*.

Campbell, Kenneth W, and Yousef Bozorgnia. 2014. "NGA-West2 Ground Motion Model for the Average Horizontal Components of PGA, PGV, and 5% Damped Linear Acceleration Response Spectra." *Earthquake Spectra* 30(3): 1087–1115. http://earthquakespectra.org/doi/10.1193/062913EQS175M (April 26, 2016).

Chandramohan, Reagan, Jack W Baker, and Gregory G Deierlein. 2016. "Quantifying the Influence of Ground Motion Duration on Structural Collapse Capacity Using Spectrally Equivalent Records." *Earthquake Spectra* 32(2): 927–50. http://earthquakespectra.org/doi/10.1193/122813EQS298MR2 (July 24, 2016).

Chang, S W, A D Frankel, and C S Weaver. 2014. *Report on Workshop to Incorporate Basin Response in the Design of Tall Buildings in the Puget Sound Region, Washington.*

Charney, Finley A. 1990. "Wind Drift Serviceability Limit State Design of Multistory Buildings." *Journal of Wind Engineering and Industrial Aerodynamics* 36: 203–12. http://linkinghub.elsevier.com/retrieve/pii/016761059090305V.

City of Seattle Department of Planning and Developments. 2015. “Alternate Design Requirements for Use of Special Reinforced Concrete Shear Walls in Over Height Buildings.” http://www.seattle.gov/dpd/codes/dr/DR2015-5.pdf (April 21, 2018).

Clough, R. W., and J. Penzien. 2010. *Dynamics of Structures*. Computers and Structures inc; 2nd Revised edition (2010).

Coffin, L. F., Jr. 1971. “A Note on Low Cycle Fatigue Laws.” *J. Mater.* 6: 388–402.

Coffin, L. F., Jr. 1954. “A Study of the Effect of Cyclic Thermal Stresses on a Ductile Metal.” *Trans. ASME* 76: 931–50.

Coleman, J, and Enrico Spacone. 2001. “Localization Issues in Force-Based Frame Elements.” *Journal of Structural Engineering* 127(11): 1257–65. http://ascelibrary.org/doi/10.1061/%28ASCE%290733-9445%282001%29127%3A11%281257%29.

Deng, P., Pei, S., Hartzell, S., Luco, N., and Rezaeian, S. 2018. “A response spectrum-based indicator for structural damage prediction.” *Engineering Structures*, 166, 546–555.

Dilger, W. G., and S. J. Brown. 1995. *Earthquake Resistance of Slab-Column Connection*. Zurich, Switzerland.

Dilger, W., and H. Cao. 1991. “Behaviour of Slab-Column Connections under Reversed Cyclic Loading.” In *Proceedings of the Second International Conference of High-Rise Buildings*, China, 10.

Eads, Laura, Eduardo Miranda, and Dimitrios G Lignos. 2015. “Average Spectral Acceleration as an Intensity Measure for Collapse Risk Assessment.” *Earthquake Engineering & Structural Dynamics* 44(12): 2057–73. http://doi.wiley.com/10.1002/eqe.2575 (April 12, 2015).

FEMA (Federal Emergency Management Agency). 2009. *Quantification of Building Seismic Performance Factors*. Redwood, CA.

FEMA (Federal Emergency Management Agency). 2015. *NEHRP Recommended Seismic Provisions for New Buildings and Other Structures (FEMA P-1050-1/2015 Edition)*.

Frankel, A. 2009. “A Constant Stress-Drop Model for Producing Broadband Synthetic Seismograms: Comparison with the Next Generation Attenuation Relations.” *Bulletin of the Seismological Society of America* 99(2A): 664–80. http://www.bssaonline.org/cgi/doi/10.1785/0120080079 (August 2, 2016).

Frankel, A. 2013. “Rupture History of the 2011 M 9 Tohoku Japan Earthquake Determined from Strong-Motion and High-Rate GPS Recordings: Subevents Radiating Energy in Different Frequency Bands.” *Bulletin of the*

Seismological Society of America 103(2B): 1290–1306. https://pubs.geoscienceworld.org/bssa/article/103/2B/1290-1306/331584.

Frankel, A., W. Stephenson, and D. Carver. 2009. “Sedimentary Basin Effects in Seattle, Washington: Ground-Motion Observations and 3D Simulations.” *Bulletin of the Seismological Society of America* 99(3): 1579–1611. https://pubs.geoscienceworld.org/bssa/article/99/3/1579-1611/342027.

Frankel, A., E. Wirth, and N. Marafi. 2018a. “The M9 Project Ground Motions.” https://doi.org/10.17603/DS2WM3W.

Frankel, A., Wirth, E., Marafi, N., Vidale, J., and Stephenson, W. 2018b. “Broadband Synthetic Seismograms for Magnitude 9 Earthquakes on the Cascadia Megathrust Based on 3D Simulations and Stochastic Synthetics, Part 1: Methodology and Overall Results.” *Bulletin of the Seismological Society of America*.

Goldfinger, C., Nelson, C. H., Morey, A. E., Johnson, J. E., Patton, J. R., Karabanov, E., Gutiérrez-Pastor, J., Eriksson, A. T., Gràcia, E., Dunhill, G., Enkin, R. J., Dallimore, A., and Vallier, T. 2012. *Turbidite Event History—Methods and Implications for Holocene Paleoseismicity of the Cascadia Subduction Zone*.

Hancock, Jonathan, and Julian J Bommer. 2007. “Using Spectral Matched Records to Explore the Influence of Strong-Motion Duration on Inelastic Structural Response.” *Soil Dynamics and Earthquake Engineering* 27(4): 291–99. http://linkinghub.elsevier.com/retrieve/pii/S0267726106001588 (August 17, 2015).

Haselton, Curt B, Jack W Baker, Abbie B Liel, and Gregory G Deierlein. 2011a. “Accounting for Ground-Motion Spectral Shape Characteristics in Structural Collapse Assessment through an Adjustment for Epsilon.” *Journal of Structural Engineering* 137(3): 332–44. http://ascelibrary.org/doi/abs/10.1061/%28ASCE%29ST.1943-541X.0000103 (February 15, 2015).

Haselton, C. B., Liel, A. B., Deierlein, G. G., Dean, B. S., and Chou, J. H. 2011b. “Seismic Collapse Safety of Reinforced Concrete Buildings. I: Assessment of Ductile Moment Frames.” *Journal of Structural Engineering*, 137(4), 481–491.

Hueste, Mary Beth D., JoAnn Browning, Andres Lepage, and John W. Wallace. 2007. “Seismic Design Criteria for Slab-Column Connections.” *ACI Structural Journal* 104(4): 448–58.

Hueste, Mary Beth D., Thomas H.-K. Kang, and Ian N. Robertson. 2009. “Lateral Drift Limits for Structural Concrete Slab-Column Connections Including Shear Reinforcement Effects.” In *Structures Congress 2009*, Reston, VA: American Society of Civil Engineers, 1–10. http://ascelibrary.org/doi/10.1061/41031%28341%29165.

Jayaram, Nirmal, Ting Lin, and Jack W. Baker. 2011. “A Computationally Efficient Ground-Motion Selection Algorithm for Matching a Target Response Spectrum Mean and Variance.” *Earthquake Spectra* 27(3): 797–815. http://epublications.marquette.edu/cgi/viewcontent.cgi?article=1114&context=civengin_fac.

Klemencic, Ron, J. Andrew Fry, Gabriel Hurtado, and Jack P. Moehle. 2006. “Performance of Post-Tensioned Slab-Core Wall Connections.” *PTI Journal* 4(2).

Kunnath, Sashi K., YeongAe Heo, and Jon F. Mohle. 2009. “Nonlinear Uniaxial Material Model for Reinforcing Steel Bars.” *Journal of Structural Engineering* 135(4): 335–43.

Liu, P C, and R J Archuleta. 2002. “The Effect of a Low-Velocity Surface Layer on Simulated Ground Motion.” *Seismological Research Letters* 73(2): 195–272. http://srl.geoscienceworld.org/cgi/doi/10.1785/gssrl.73.2.195 (August 3, 2016).

Luco, Nicolas, and C Allin Cornell. 2007. “Structure-Specific Scalar Intensity Measures for Near-Source and Ordinary Earthquake Ground Motions.” *Earthquake Spectra* 23(2): 357–92. http://earthquakespectra.org/doi/abs/10.1193/1.2723158 (February 16, 2015).

Manson, S. S. 1965. “Fatigue: A Complex Subject-Some Simple Approximations.” *Exp. Mech.* 5(7): 193–226.

Marafi, Nasser A. 2018. “Impacts of an M9 Cascadia Subduction Zone Earthquake on Structures Located In Deep Sedimentary Basins.” University of Washington.

Marafi, Nasser A., Jeffrey W. Berman, and Marc O. Eberhard. 2016. “Ductility-Dependent Intensity Measure That Accounts for Ground-Motion Spectral Shape and Duration.” *Earthquake Engineering & Structural Dynamics* 45(4): 653–72. http://onlinelibrary.wiley.com/doi/10.1002/eqe.2678/full.

Marafi, N. A., Eberhard, M. O., Berman, J. W., Wirth, E. A., and Frankel, A. D. 2017. “Effects of Deep Basins on Structural Collapse during Large Subduction Earthquakes.” Earthquake Spectra, 33(3), 963–997.

Marafi, Nasser A., Kamal A. Ahmed, Dawn E. Lehman, and Laura N. Lowes. 2019a. “Variability in Seismic Collapse Probabilities of Solid and Coupled-Wall Buildings.” *Journal of Structural Engineering, in-press*.

Marafi, N. A., Eberhard, M. O., Berman, J. W., Wirth, E. A., and D., F. A. 2019b. “Impacts of Simulated M9 Cascadia Subduction Zone Motions on Idealized Systems.” *Earthquake Spectra, in-press*.

Marsh, M. Lee, and Christopher M. Gianotti. 1995. “Inelastic Structural Response to Cascadia Subduction Zone Earthquakes.” *Earthquake Spectra* 11(1): 63–89. http://earthquakespectra.org/doi/10.1193/1.1585803.

Matzke, Eric M., Rémy D. Lequesne, Gustavo J. Parra-Montesinos, and Carol K. Shield. 2015. “Behavior of Biaxially Loaded Slab-Column Connections with Shear Studs.” *ACI Structural Journal* 113(3): 335–46.

McKenna, F. 2016. “OpenSees.” http://opensees.berkeley.edu/ (April 24, 2018).

Megally, S., and A. Ghali. 2000. “Punching Shear Design of Earthquake-Resistant Slab-Column Connections.” *ACI Structural Journal* 97(5): 720–30.

Miner, M. A. 1945. “Cumulative Damage in Fatigue.” *J. Appl. Mech.* 12: A159–A164.

Morikawa, N, and H Fujiwara. 2013. “A New Ground Motion Prediction Equation for Japan Applicable up to M9 Mega-Earthquake.” *Journal of Disaster Research* 8(5): 878–88. https://www.fujipress.jp/jdr/dr/dsstr000800050878 (April 22, 2016).

PEER. 2017. *Tall Building Initiative: Guidelines for Performance-Based Seismic Design of Tall Buildings*. Berkeley, CA. http://peer.berkeley.edu/news/2017/05/new-peer-report-201706-guidelines-for-performance-based-seismic-design-of-tall-buildings-version-2-0/.

Petersen, M D, C H Cramer, and A D Frankel. 2002. “Simulations of Seismic Hazard for the Pacific Northwest of the United States from Earthquakes Associated with the Cascadia Subduction Zone.” *Pure and Applied Geophysics* 159(9): 2147–68. http://link.springer.com/10.1007/s00024-002-8728-5 (September 24, 2016).

Petersen, M. D., Moschetti, M. P., Powers, P. M., Mueller, C. S., Haller, K. M., Frankel, A. D., Zeng, Y., Rezaeian, S., Harmsen, S. C., Boyd, O. S., Field, N., Chen, R., Rukstales, K. S., Luco, N., Wheeler, R. L., Williams, R. A., and Olsen, A. H. 2014. *Documentation for the 2014 Update of the United States National Seismic Hazard Maps*.

Popovics, Sandor. 1973. “A Numerical Approach to the Complete Stress-Strain Curve of Concrete.” *Cement and Concrete Research* 3(5): 583–99.

Pugh, Joshua S., Laura N. Lowes, and Dawn E. Lehman. 2015. “Nonlinear Line-Element Modeling of Flexural Reinforced Concrete Walls.” *Engineering Structures* 104: 174–92. http://linkinghub.elsevier.com/retrieve/pii/S0141029615005428.

Raghunandan, Meera, Abbie B Liel, and Nicolas Luco. 2015. "Collapse Risk of Buildings in the Pacific Northwest Region Due to Subduction Earthquakes." *Earthquake Spectra* 31(4): 2087–2115. http://earthquakespectra.org/doi/10.1193/012114EQS011M (October 7, 2016).

Saatcioglu, Murat, and Salim R Razvi. 1992. "Strength and Ductility of Confined Concrete." *Journal of Structural Engineering* 118(6): 1590–1607.

Shahi, S. K., and J. W. Baker. 2011. "An Empirically Calibrated Framework for Including the Effects of Near-Fault Directivity in Probabilistic Seismic Hazard Analysis." *Bulletin of the Seismological Society of America* 101(2): 742–55. https://pubs.geoscienceworld.org/bssa/article/101/2/742-755/349560.

Stephenson, William J, Nadine G Reitman, and Stephen J Angster. 2017. Open-File Report *P- and S-Wave Velocity Models Incorporating the Cascadia Subduction Zone for 3D Earthquake Ground Motion Simulations—Update for Open-File Report 2007–1348*. Version 1. Reston, VA. http://pubs.er.usgs.gov/publication/ofr20171152.

Structural Engineers Association of Washington. (2018, January 9th). Earthquake Engineering Committee meeting.

Wirth, E. A., Frankel, A. D., Marafi, N., Vidale, J. E., and Stephenson, W. J. 2018. "Broadband Synthetic Seismograms for Magnitude 9 Earthquakes on the Cascadia Megathrust Based on 3D Simulations and Stochastic Synthetics, Part 2: Rupture Parameters and Variability." *Bulletin of the Seismological Society of America*.

Wong, P. S., F. J. Vecchio, and H. Trommels. 2013. *VECTOR2 & FORMWORKS USER'S MANUAL*. http://www.civ.utoronto.ca/vector/user_manuals/manual1.pdf.

Yassin, Mohd Hisham Mohd. 1994. "Nonlinear Analysis of Prestressed Concrete Structures under Monotonic and Cyclic Loads." University of California, Berkeley.

Appendix A: Archetype Key Characteristics

Archetype Characteristics

Thirty two core-wall archetypes were designed, ranging from 4- to 40-stories tall, using ASCE 7-10 and ASCE 7-16 based on the methodology described in the paper. Table A1 and A2 summarizes the core length (l_w), core width (b_w), and wall thickness (t_w) for code enhanced and code minimum archetypes, respectively. For all archetypes 8-stories and taller the longitudinal reinforcement ratio (ρ_l) at various story ranges is summarized in Table A1 and A2. Note that the four-story archetypes were designed as a planar wall with boundary elements (i.e., $b_w = t_w$). The boundary element length sizes (l_{be}) and longitudinal reinforcement ratios ($\rho_{l,be}$) are summarized in Table A3 for all 4-story archetypes. Minimum longitudinal reinforcement was used in the web region as permitted by ACI 318, where the reinforcement area equaled 0.25% of the wall cross-section area.

The wall's longitudinal reinforcement was tied in the transverse direction and detailed according to the requirements in ACI 318-14 §18.10. The transverse reinforcement ratio is summarized in column ρ_v in Table A1. The variation in wall reinforcement layout along the wall height was optimized to balance efficiency (the required versus the provided reinforcement) and constructability (the number of variations in the section reinforcement layout).

Table A1. Archetype dimensions and reinforcement layout for Code Enhanced Archetypes

Arch. ID	Stories	l_w *(in)*	b_w *(in)*	t_w *(in)*	ρ_l	ρ_v	Arch. ID	Stories	l_w *(in)*	b_w *(in)*	t_w *(in)*	ρ_l	ρ_v
S4-10-E	-1 to 4	168	0	14	-	-	S4-16-E	-1 to 4	192	0	18	-	-
S8-10-E	-2 to 3	192	96	14	0.90	1.37	S8-16-E	-2 to 3	216	108	16	0.95	1.65
S8-10-E	4 to 6	192	96	14	0.55	0.82	S8-16-E	4 to 6	216	108	16	0.70	1.19
S8-10-E	7 to 8	192	96	14	0.25	0.25	S8-16-E	7 to 8	216	108	16	0.25	0.25
S12-10-E	-3 to 3	240	120	14	0.50	1.49	S12-16-E	-3 to 3	240	120	18	0.85	2.27
S12-10-E	4 to 6	240	120	14	0.50	0.75	S12-16-E	4 to 6	240	120	18	0.60	0.80
S12-10-E	7 to 9	240	120	14	0.35	0.25	S12-16-E	7 to 9	240	120	18	0.40	0.25
S12-10-E	10 to 12	240	120	14	0.25	0.25	S12-16-E	10 to 12	240	120	18	0.25	0.25
S16-10-E	-3 to 4	264	132	14	0.50	1.04	S16-16-E	-3 to 4	288	144	22	0.60	1.44
S16-10-E	5 to 8	264	132	14	0.50	0.75	S16-16-E	5 to 8	288	144	22	0.50	0.81
S16-10-E	9 to 16	264	132	14	0.25	0.25	S16-16-E	9 to 12	288	144	22	0.40	0.25
S20-10-E	-3 to 4	288	144	14	0.50	1.04	S16-16-E	13 to 16	288	144	22	0.25	0.25
S20-10-E	5 to 8	288	144	14	0.50	0.75	S20-16-E	-3 to 4	312	156	24	0.55	1.44
S20-10-E	9 to 12	288	144	14	0.35	0.25	S20-16-E	5 to 8	312	156	24	0.50	1.28
S20-10-E	13 to 20	288	144	14	0.25	0.25	S20-16-E	9 to 12	312	156	24	0.450	0.25
S24-10-E	-3 to 4	312	156	18	1.00	1.96	S20-16-E	13 to 16	312	156	24	0.25	0.25
S24-10-E	5 to 8	312	156	18	0.75	1.00	S20-16-E	17 to 20	304	156	20	0.25	0.25
S24-10-E	9 to 12	312	156	18	0.60	0.80	S24-16-E	-3 to 4	336	168	26	1.10	2.38
S24-10-E	13 to 16	312	156	18	0.50	0.96	S24-16-E	5 to 8	336	168	26	0.75	1.06
S28-10-E	17 to 20	304	156	14	0.50	0.75	S24-16-E	9 to 12	336	168	26	0.60	1.16
S28-10-E	21 to 24	304	156	14	0.50	0.25	S28-16-E	13 to 16	336	168	26	0.50	0.96
S28-10-E	-3 to 4	336	168	18	0.85	1.67	S28-16-E	17 to 24	328	168	22	0.50	0.81
S32-10-E	5 to 8	336	168	18	0.60	0.80	S28-16-E	-3 to 4	360	180	28	0.95	2.90
S32-10-E	9 to 16	336	168	18	0.50	0.67	S28-16-E	5 to 8	360	180	28	0.70	1.07
S32-10-E	17 to 28	332	168	16	0.50	0.59	S32-16-E	9 to 12	360	180	28	0.60	1.24
S36-10-E	-3 to 4	360	180	20	0.75	2.22	S32-16-E	13 to 16	360	180	28	0.50	1.04
S36-10-E	5 to 16	360	180	20	0.50	0.74	S32-16-E	17 to 28	352	180	24	0.50	0.89
S36-10-E	17 to 32	356	180	18	0.50	0.67	S32-16-E	-3 to 4	384	192	30	0.95	3.10
S40-10-E	-3 to 4	384	192	22	0.60	1.96	S32-16-E	5 to 8	384	192	30	0.80	1.31
S40-10-E	5 to 16	384	192	22	0.50	0.81	S36-16-E	9 to 12	384	192	30	0.70	1.14
S40-10-E	17 to 36	372	192	16	0.50	0.59	S36-16-E	13 to 16	384	192	30	0.50	1.60
S40-10-E	-3 to 4	408	204	24	0.60	2.13	S36-16-E	17 to 32	376	192	26	0.50	0.96
S40-10-E	5 to 8	408	204	24	0.60	1.07	S36-16-E	-3 to 4	408	204	32	1.10	2.93
							S36-16-E	5 to 8	408	204	32	0.80	1.07
							S40-16-E	9 to 12	408	204	32	0.70	1.22
							S40-16-E	13 to 16	408	204	32	0.60	1.04
							S40-16-E	17 to 36	400	204	28	0.50	1.04
							S40-16-E	-3 to 4	432	216	34	1.20	3.4
							S40-16-E	5 to 8	432	216	34	1.00	1.42
							S40-16-E	9 to 12	432	216	34	0.80	1.48
							S40-16-E	13 to 16	432	216	34	0.80	2.01

Table A2. Archetype dimensions and reinforcement layout for Code Minimum Archetypes

Arch. ID	Stories	l_w (in)	b_w(in)	t_w(in)	ρ_l	ρ_v	Arch. ID	Stories	l_w(in)	b_w(in)	t_w(in)	ρ_l	ρ_v
S4-10-M	-1 to 4	120	0	14	-	-	S4-16-M	-1 to 4	144	0	18	-	-
S8-10-M	-2 to 3	132	66	20	2.00	3.33	S8-16-M	-2 to 3	144	72	24	2.00	4.00
S8-10-M	4 to 6	132	66	20	1.10	0.92	S8-16-M	4 to 6	144	72	24	1.00	1.00
S8-10-M	7 to 8	132	66	20	0.25	0.25	S8-16-M	7 to 8	144	72	24	0.25	0.25
S12-10-M	-3 to 3	168	84	20	1.60	2.67	S12-16-M	-3 to 3	180	90	24	1.60	3.20
S12-10-M	4 to 6	168	84	20	1.00	0.83	S12-16-M	4 to 6	180	90	24	1.20	1.20
S12-10-M	7 to 9	160	84	16	0.45	0.25	S12-16-M	7 to 9	168	90	18	0.70	2.10
S12-10-M	10 to 12	160	84	16	0.25	0.25	S12-16-M	10 to 12	168	90	18	0.25	0.25
S16-10-M	-3 to 4	192	96	22	1.40	2.57	S16-16-M	-3 to 4	204	102	28	1.50	3.50
S16-10-M	5 to 8	192	96	22	1.00	0.92	S16-16-M	5 to 8	204	102	28	1.00	1.17
S16-10-M	9 to 12	180	96	16	0.35	0.25	S16-16-M	9 to 12	188	102	20	0.60	1.28
S16-10-M	13 to 16	180	96	16	0.25	0.25	S16-16-M	13 to 16	188	102	20	0.25	0.25
S20-10-M	-3 to 4	216	108	24	1.20	2.40	S20-16-M	-3 to 4	228	114	30	1.40	2.77
S20-10-M	5 to 8	216	108	24	0.90	0.90	S20-16-M	5 to 8	228	114	30	0.95	1.19
S20-10-M	9 to 12	204	108	18	0.50	1.50	S20-16-M	9 to 12	212	114	22	0.70	1.14
S20-10-M	13 to 20	204	108	18	0.25	0.25	S20-16-M	13 to 20	212	114	22	0.25	0.25
S24-10-M	-3 to 4	252	126	28	0.70	4.18	S24-16-M	-3 to 4	252	126	32	1.30	2.74
S24-10-M	5 to 8	252	126	28	0.50	1.49	S24-16-M	5 to 8	252	126	32	1.10	1.47
S24-10-M	9 to 12	232	126	18	0.50	1.50	S24-16-M	9 to 12	240	126	26	0.80	1.13
S24-10-M	13 to 24	232	126	18	0.25	0.25	S24-16-M	13 to 16	240	126	26	0.35	0.25
							S24-16-M	17 to 24	240	126	26	0.25	0.25

Table A3. Boundary element information for the 4-story archetypes.

Archetype ID	Stories	l_{be} (in)	$\rho_{l,be}$
S4-10-E	-1 to 2	42”	0.030
S4-10-E	2 to 4	26”	0.030
S4-16-E	-1 to 2	54”	0.023
S4-16-E	2 to 4	34”	0.023
S4-10-M	-1 to 2	58”	0.029
S4-10-M	2 to 4	26”	0.030
S4-16-M	-1 to 2	50”	0.037
S4-16-M	2 to 4	42”	0.037

Appendix B. Archetype Modeling

For all walled buildings, the seismic performance was assessed using 2D models in OpenSees (McKenna, 2016) with earthquake demands applied only in one direction. Figure B.1 shows a schematic of the OpenSees models where the walls were modeled using six displacement-based beam-column elements (DBE) per story, with five integration points per element and applying the Gauss-Lobatto numerical integration scheme. The axial and flexural response of each RC cross-section was modeled using a fiber-based approach at each integration point. To account for shear deformations along the wall height, each DBE included a shear spring. Figure B.1.c illustrates the fiber cross-section for the walls.

CONSTITUTIVE MODELING

Constitutive models are shown in Figure B.2. Expected concrete and steel material strengths were defined as $f'_{ce} = 1.3f'_c$ and $f_{ye} = 1.17f_y$, respectively, per PEER TBI (2017). A modified version of the OpenSees *Steel02* material model was used to simulate the cyclic response of reinforcing steel that accounts for cyclic strength-deterioration (Kunnath et al. 2009). This material model called *Steel02Fatigue* herein, uses the stress-strain backbone curve and unload/reload paths are defined using the model by Menegotto and Pinto (1973). The cumulative strength degradation of the material is based on the model by the Coffin (1954, 1971) and Manson (1965) fatigue life expression and Miner's (1945) linear damage rule. A detailed discussion of this is implementation can be found in Kunnath et al. (2009). The reinforcing bar assumed a modulus of elasticity, E_s = 200 GPa (29,000 ksi), a constant post-yield strain-hardening ratio of 0.6% (shown as parameter b in Figure B.2). For the *Steel02Fatigue* material, the deterioration parameters C_d, C_f, α, and β were taken as 0.2, 0.12, 0.44, and 0.45, respectively, as recommended by Kunnath et al. (2009). Figure B.3a compares the stress-strain response of *Steel02* and *Steel02Fatigue* illustrating the cyclic degradation of strength.

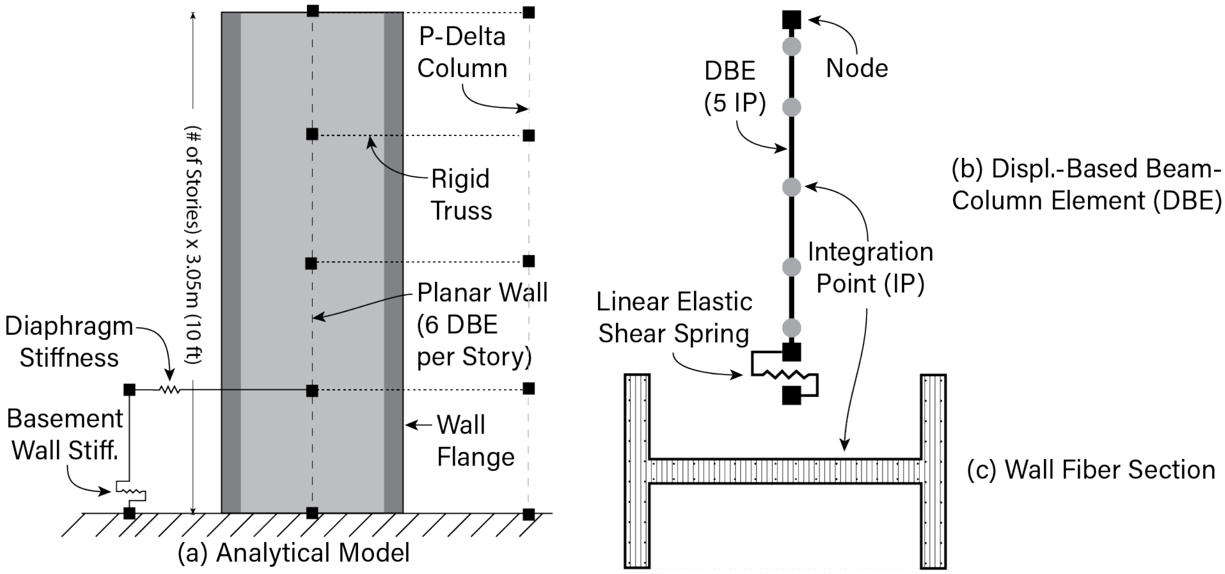

Figure B.1. Diagram of the (a) OpenSees analytical model, (b) wall element modeled using displacement-based elements, and (c) wall fiber section.

The longitudinal reinforcing bars inside RC members exhibit excessive buckling once the surrounding concrete crushes. Pugh developed a simple model to simulate full bar buckling, using the OpenSees *MinMax* wrapper that forced the reinforcing steel to lose compression and tension strength once the surrounding concrete reaches residual strain (ε_{res} in Figure B.2). To simulate tensile fracture of the reinforcing bars, the *MinMax* wrapper forced the material to lose strength once the strains exceed the ultimate tensile strain, ε_u, taken as 20%.

For concrete materials, a modified version of the OpenSees *Concrete02* material model (Yassin, 1994) was used to simulate the cyclic response of the concrete. This material model is called *Concrete02IS* herein, was modified to use Popovics (1973) pre-peak stress-strain relationship that enabled the user to specify an initial elastic stiffness (E_c) of the concrete irrespective of the peak-stress and strain (shown in Figure B.3b). For post-peak stress-strain response, the stresses were assumed to be linear from peak-stress (f_p) to the residual concrete capacity (f_{res}) as shown in Figure B.2b. The strain at maximum stress is denoted as ε_p. For unconfined concrete, ε_p was set as $2f_p/E_c$ where E_c is defined as $4{,}750\sqrt{f_p}$ MPa ($57{,}000\sqrt{f_p}$ psi, as recommended by ACI 318-14). For the base model, the confined concrete variables $f_p = f'_{cce}$ and ε_p were defined using recommendations by Saatcioglu and Razvi (1992). The residual concrete capacity, f_{res}, was taken as βf_p where β is defined as 0.01 for unconfined concrete and 0.2 for confined concrete. The tensile strength equaled $0.33\sqrt{f'_{ce}}$ MPa ($4\sqrt{f'_{ce}}$ psi, as per Wong et al. 2013) and a tensile softening stiffness (E_t) equaled 0.05 E_c (Yassin, 1994). The parameter λ in *Concrete02* was taken as 0.1, which is the ratio of unloading slope at ε_p to E_c.

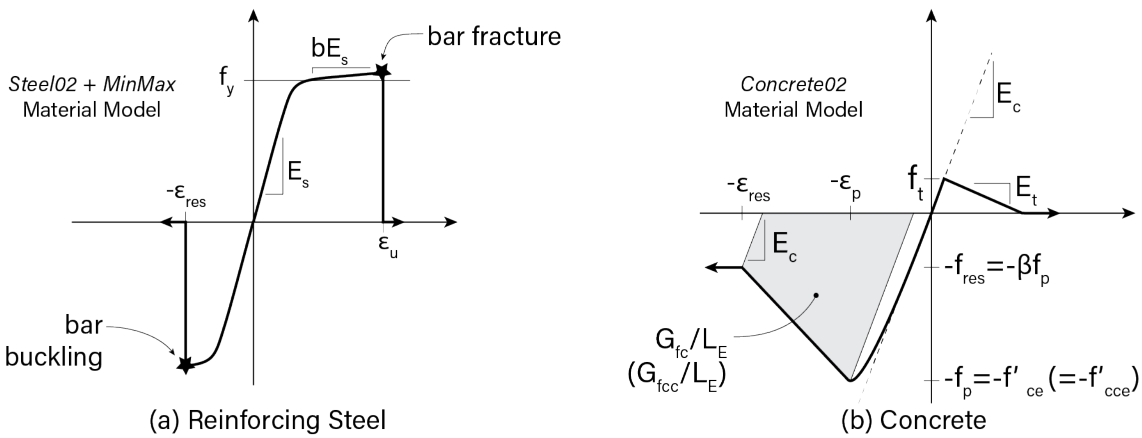

Figure B.2. Stress-strain relationship for the fiber-section (a) reinforcing steel and (b) concrete. Confined concrete properties are shown in parenthesis.

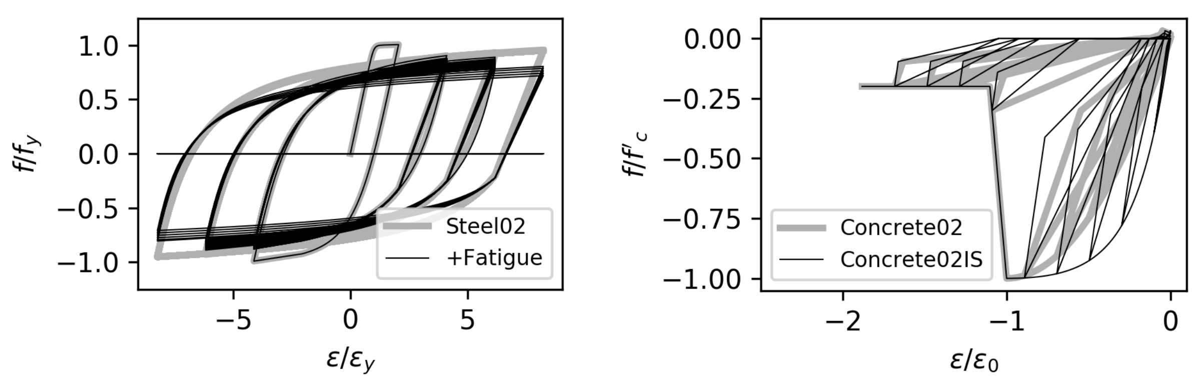

Figure B.3. Stress-strain response of a modified OpenSees (a) *Steel02* model that accounts for cyclic strength degradation based on Kunnath et al. 2009 and (b) *Concrete02* model with revised pre-peak properties.

Birely (2012) showed that the majority of walls sustain a compression-type failure characterized by simultaneous concrete crushing and buckling of the longitudinal reinforcement. Coleman & Spacone, (2001) and Pugh et al. (2015) showed that when wall failure occurs and accompanying strength loss is simulated, deformations localize in the failing element or section, which results in "mesh-dependent" results if steps are not taken to mitigate this. To minimize mesh dependences, work by Coleman & Spacone (2001) and Pugh et al. (2015) regularized concrete compression softening with the post-peak concrete compression stress-strain response using the concrete compressive energy (G_f) and a measure of the element mesh size. Specifically, regularized strain at onset of residual compressive strength, ε_{res}, shown in Figure B.2 was computed as,

$$\varepsilon_{res} = \frac{2G_f}{(\beta+1)f_p L_e} + \varepsilon_p \frac{\beta+1}{2} \tag{B.1}$$

where G_f is defined as the concrete crushing energy in N/mm (kips per in), β is the percentage of f_p corresponding to the residual compressive strength, and L_E is the length over which softening occurs in the model. For DBE, L_E is length of the entire element because the DBE formulations forces localization within a single element (Coleman & Spacone, 2001). The optimal value of G_f was determined in Marafi et al. (2019a) and taken as $2.0f'_{ce}$ N/mm ($0.0134f'_{ce}$ kips/in) and $3.5f'_{ce}$ N/mm ($0.0268f'_{ce}$ kips/in) for unconfined and confined concrete, respectively.

Shear deformations were modeled using a linear spring, as shown in Figure B.1. The elastic shear stiffness of a cantilevered column can be estimated as GA_v/L_E where G is the shear modulus, A_v is the effective shear area, and L_E is the length of the wall element. This paper approximates G as $0.4E_c$, as per ACI 318-14, and A_v is taken as $0.83A_g$, where A_g is the gross cross-sectional area of the web. The resulting shear stiffness equaled $0.33E_cA_g$ which is between the recommended value from TBI ($0.2E_cA_g$) and from ASCE 41-13 (2014, $0.4E_cA_g$). Changes in the shear stiffness did not affect the overall archetype performance because the core walls are flexure controlled.

OTHER MODELLING ASSUMPTIONS

A P-delta column was used to model the effects of the gravity system, as shown in Figure B.3, connected to the RC wall using rigid-truss elements at every story. The P-delta column is a rigid axial element with a pinned support. The vertical load resisted by the P-Delta column at each level is a percentage of the floor area resisted by the gravity system multiplied by the total seismic weight resisted by the wall (i.e., the remainder of the archetype's total vertical load due to gravity not resisted by the wall). The OpenSees models used modal damping and supplemented with stiffness-only Rayleigh damping to dampen the dynamic amplifications associated with higher mode effects (Clough and Penzien 2010). The number of modes that were dampened was equal to the total number of stories, N, where the total damping (modal plus stiffness-only Rayleigh) in each mode equaled to 2.5%, as recommended by the TBI 2017.

The retaining walls and basement-level diaphragms were modelled using elastic spring element shown in Figure B.3. The diaphragm stiffnesses (axial spring shown in Figure B.3) and basement wall stiffnesses (shear spring shown in Figure B.3) were estimated using a 3-dimensional elastic finite-element model. The basement walls were 305 mm (12 in) thick by 48.8 m (160 ft) long retaining walls around the basement wall perimeter (shown in Figure 7) connected to a 356 mm (14 in) thick basement slab at the ground level and 254 mm (10 in) thick at levels below ground. The elastic properties of the retaining wall and diaphragms was estimated as per the recommendation in the TBI 2017 where the basement wall used flexural and shear stiffness equal to $0.8E_cI_g$ and $0.2E_cA_g$, respectively, and the diaphragm axial and shear stiffness is equal to $0.25E_cA_g$ and $0.25E_cI_g$, respectively.